Correspondence to:
E. H. Madden and A.-A. Gabriel,
betsymadden@gmail.com;
GABRIEL@GEOPHYSIK.
UNI-MUENCHEN.DE

The State of Pore Fluid Pressure and 3-D Megathrust Earthquake Dynamics

Elizabeth H. Madden[1,2] , **Thomas Ulrich[2]** , and **Alice-Agnes Gabriel[2,3]**

[1]Observatório Sismológico, Instituto de Geociências, Universidade de Brasília, Brasília, Brazil, [2]Department of Earth and Environmental Sciences, Ludwig-Maximilians-Universität München, Munich, Germany, [3]Institute of Geophysics and Planetary Physics, Scripps Institution of Oceanography, University of California San Diego, La Jolla, CA, USA

Abstract We study the effects of pore fluid pressure (P_f) on the pre-earthquake, near-fault stress state, and 3-D earthquake rupture dynamics through six scenarios utilizing a structural model based on the 2004 M_w 9.1 Sumatra-Andaman earthquake. As pre-earthquake P_f magnitude increases, effective normal stress and fault shear strength decrease. As a result, magnitude, slip, peak slip rate, stress drop, and rupture velocity of the scenario earthquakes decrease. Comparison of results with observations of the 2004 earthquake support that pre-earthquake P_f averages near 97% of lithostatic pressure, leading to pre-earthquake average shear and effective normal tractions of 4–5 and 22 MPa. The megathrust in these scenarios is weak, in terms of low mean shear traction at static failure and low dynamic friction coefficient during rupture. Apparent co-seismic principal stress rotations and absolute post-seismic stresses in these scenarios are consistent with the variety of observed aftershock focal mechanisms. In all scenarios, the mean apparent stress rotations are larger above than below the megathrust. Scenarios with larger P_f magnitudes exhibit lower mean apparent principal stress rotations. We further evaluate pre-earthquake P_f depth distribution. If P_f follows a sublithostatic gradient, pre-earthquake effective normal stress increases with depth. If P_f follows the lithostatic gradient exactly, then this normal stress is constant, shifting peak slip and peak slip rate updip. This renders constraints on near-trench strength and constitutive behavior crucial for mitigating hazard. These scenarios provide opportunity for future calibration with site-specific measurements to constrain dynamically plausible megathrust strength and P_f gradients.

Plain Language Summary Large volumes of fluid can lead to high-pressures that weaken rocks in fault zones and influence earthquake rupture. While fluids are critical to understanding behavior at subduction zones, where the largest earthquakes in the world occur and where tsunami generation increases hazard, measuring fluid and fluid pressure directly across an entire megathrust currently is not possible. Here, we use supercomputers to model the devastating 2004 M_w 9.1 Sumatra-Andaman earthquake in 3-D in order to isolate the role of fluid pressure on earthquake behavior. By first building a reliable base model and then varying fluid pressure to generate six earthquake scenarios, we find that fluid pressure is likely very high, and also that the way that fluid pressure varies with depth can greatly influence the earthquake and associated hazard. Fluid pressure controls location of the largest and fastest fault slip along the megathrust, and the possibility for a devastating tsunami.

1. Introduction

High pore fluid pressures in subduction zones are expected due to the low rates of diffusion and the numerous geologic processes that produce fluids (Saffer & Tobin, 2011). Indications of overpressure, when pore fluid pressure (P_f) is above the hydrostatic pressure gradient, include observations of extensional veining (Rowe et al., 2009) and high seismic reflectivity (e.g., Calahorrano et al., 2008). These observations indicate P_f at 75% of the lithostatic load at Nankai (Tobin & Saffer, 2009), while shallow boreholes indicate P_f at up to 97% of the lithostatic pressure (Saffer & Tobin, 2011). At Cascadia, high ratios of P wave to S wave speed (V_p/V_s) observed from receiver functions are inconsistent with lithology, but can be explained by near-lithostatic P_f (Audet et al., 2009).

P_f differences are thought to explain spatial and temporal variations in slip behavior observed in subduction zones (e.g., Audet & Schwartz, 2013; Gao & Wang, 2017; Saffer, 2017; Saffer & Tobin, 2011). At the base of the seismogenic zone, high P_f is linked to low effective normal stress conditions and slow earthquake slip behavior (Bürgmann, 2018; Liu & Rice, 2007; Rice, 2006; Shelly et al., 2007). Slow slip earthquakes observed deep along

the Cascadia subduction zone are attributed to hydrofracturing of the barrier trapping fluids in the down-going plate, allowing fluids to circulate (Audet et al., 2009). Fluid circulation under high-pressure also may be responsible for low-frequency tremor and rapid tremor migration (Beeler et al., 2013; Cruz-Atienza et al., 2018). Tremor in the Japan Trench is co-located with regions of high P_f (Shelly et al., 2006). Deep tremor at the Livingstone Fault in New Zealand appears co-located with regions of high P_f caused by serpentinite reactions near the slab-mantle interface (Tarling et al., 2019). Both tremor and slow slip have been linked to the very small changes in pressure from tidal stress, suggesting weak faults and high P_f (Houston, 2015; Tonegawa et al., 2021).

In seismogenic regions of subduction zones, lower P_f conditions have been proposed as a mechanism for locking (Saffer & Tobin, 2011). Heise et al. (2017) co-locate a geodetically identified locked region with a patch of high electrical resistivity attributed to lack of fluid or low P_f on the Hikurangi subduction interface, while shallow creep occurs in a region of conductivity that can be explained by high fluid production or high P_f (Heise et al., 2013). However, heat flow studies (Gao & Wang, 2014) and force-balance inversions (Lamb, 2006) find shear to normal stress ratios that indicate high P_f near the megathrust. Lamb (2006) finds evidence for P_f at 95% of the lithostatic pressure at 7 of 9 subduction zones, including Sumatra. Two exceptions to this are Northern Chile and Tonga, with P_f at 81% of the lithostatic pressure.

Temporal variation in P_f is central to the fault-valve model of Sibson (1992, 1994), which attributes earthquakes to both tectonic loading (shear stress building until an earthquake occurs) and fluid-pressure cycling (P_f building and effective normal stress falling over time until an earthquake occurs). Petrini et al. (2020) show that fluid pressure variations in time can control subduction zone seismic cycling. Analyses of borehole fluids suggest cycles of 10,000–100,000 yr (Saffer & Tobin, 2011), which may correlate with fault formation, while shorter period variations correlate with slow slip events in Costa Rica. In addition, observed increases in V_p/V_s following the 1995 M 8 Antofagasta earthquake (Husen & Kissling, 2002) suggest the rapid movement of fluid during or directly after megathrust earthquakes. Eberhart-Phillips et al. (1989) note that such changes can occur only when P_f is near-lithostatic.

This variety of observations and inferences about P_f in subduction zones is reflected in the variety of ways that P_f is considered in faulting and earthquake models. Quasistatic models of fault slip may not incorporate P_f explicitly, but set stress gradients that produce reasonable fault slip distributions (e.g., Madden et al., 2013; Madden & Pollard, 2012). Models of earthquake sequences and rupture dynamics commonly prescribe normal stress following effective stress theory as $\sigma_n - P_f$, where σ_n is the normal stress (Brace & Kohlstedt, 1980; Hubbert & Rubey, 1959). P_f typically increases with depth and is chosen ad-hoc to help reconcile realistic earthquake characteristics with friction and fault shear strength (Kozdon & Dunham, 2013; Liu & Rice, 2005; Ulrich, Gabriel, et al., 2019; Wollherr et al., 2019). Ulrich et al. (2022) and Uphoff et al. (2017) incorporate near-lithostatic P_f following depth-dependent gradients into large-scale, three-dimensional (3-D) dynamic rupture models. Others initialize dynamic rupture models with conditions, including initial P_f, from geodynamic and seismic cycling modeling that capture long-term subduction zone deformation and fluid flow (Madden et al., 2021; Wirp et al., 2021; van Zelst et al., 2019).

Rice (1992) shows that fluid at elevated pressures within a fault zone may follow the same gradient with depth as the lithostatic stress, causing constant effective normal stress with depth. Data from crustal sedimentary rocks support this theory (Suppe, 2014). This condition is assumed in some dynamic rupture models (e.g., Ramos & Huang, 2019; Ramos et al., 2021), but not others (e.g., Kozdon & Dunham, 2013; Lotto et al., 2019; Ulrich et al., 2022; Ulrich, Vater, et al., 2019). Other models consider the coupled, dynamic effects of fluids, such as dilatancy (e.g., Aochi et al., 2014; Segall & Rice, 1995) and thermal pressurization (e.g., Garagash, 2012; Rice, 2006; Schmitt et al., 2011; Segall & Bradley, 2012). Recent two-dimensional (2-D) antiplane earthquake sequence modeling by Zhu et al. (2020) couples earthquake and pore fluid dynamics by incorporating fluid migration and periodic P_f variations over earthquake cycles. These models produce fluid-driven aseismic slip at the base of the seismic zone, large earthquakes, and earthquake swarms. 2-D seismo-hydro-mechanical modeling of subduction zone earthquake cycling shows high P_f moving progressively updip due to compaction inside an evolving fault, eventually leading to a seismic event (Petrini et al., 2020).

P_f prior to an earthquake can be constrained by these observations and inferences with simultaneous consideration of the normal stress and static frictional strength of a megathrust, but it has not been measured directly and little data is available, particularly deep along subduction zones. Few studies integrate knowledge about

megathrust mechanics with megathrust earthquake rupture dynamics to study P_f at the time of rupture. Specifically, 3-D dynamic simulations at the megathrust scale that take realistic slab geometries into account remain challenging. To supplement this gap, we explore the dynamic effects of different hypotheses about P_f magnitude and gradient in megathrust systems using a 3-D dynamic earthquake rupture and seismic wave propagation model that matches near- and far-field seismic, geodetic, geologic, and tsunami observations of the 2004 Sumatra-Andaman earthquake and Indian Ocean tsunami (Ulrich et al., 2022; Uphoff et al., 2017).

Our focus is to highlight the effects of pre-earthquake P_f conditions on earthquake behavior within a structurally complex megathrust system. We analyze how various hypotheses on P_f magnitude and depth gradient affect the pre-earthquake stress state near a megathrust, the subsequent earthquake rupture characteristics, and the postseismic stress field. Specifically, we generate six scenario earthquakes with P_f magnitudes at 31%, 62%, 93%, and 97% of the lithostatic pressure and under two different depth gradients that cause either increasing or constant normal stress near the megathrust. We compare results against observations of the 2004 earthquake as well as general observational inferences about subduction zone earthquakes.

We note that the range of pre-earthquake conditions captured by our six scenarios may reflect the variety of conditions present along a single megathrust at the same time, due to spatial variations in P_f magnitude and/or gradient. In addition, hydromechanical processes likely vary in space and time as a consequence of rock deformation processes that modulate the permeability of both fault and host rocks, in turn affecting fluid diffusion. Coupling these processes during the full seismic cycle to determine realistic fluid conditions at the start of earthquake rupture is a clear future step. However, modeling these processes in 3-D is beyond the state of the art, despite the recent progress of 2-D numerical models reviewed above. Our results provide key advances regarding the influence of P_f on earthquake behavior and provide opportunity for future calibration with site-specific friction and pore-fluid measurements to constrain dynamically plausible megathrust strength and P_f gradients.

2. Modeling Methods

2.1. Computational Model

The earthquake models are performed with SeisSol (www.seissol.org), a software package that solves for dynamic fault rupture and seismic wave propagation with high-order accuracy in space and time. SeisSol solves the seismic wave equation in velocity-stress formulation using an Arbitrary high-order DERivate Discontinuous Galerkin (ADER-DG) scheme (Dumbser & Käser, 2006). Computational optimizations target supercomputers with many-core CPUs (Breuer et al., 2014; Heinecke et al., 2014; Krenz et al., 2021; Rettenberger et al., 2016). SeisSol uses local time stepping, which increases runtime efficiency by decreasing dependence of the time-step on the element with the smallest radius (Breuer et al., 2016; Uphoff et al., 2017; Wolf et al., 2020). Following the SCEC/USGS Dynamic Rupture Code Verification exercises (Harris et al., 2018, 2009), SeisSol has been validated against several community benchmarks (De La Puente et al., 2009; Pelties et al., 2012, 2014; Wollherr et al., 2018).

2.2. Structural Model

The structural model and computational mesh are shown in Figure 1. Use of an unstructured tetrahedral mesh allows for a realistic representation of the non-planar slab interface, splay faults, curved oceanic crust, and high-resolution bathymetry. The megathrust geometry follows Slab1.0 (Hayes et al., 2012). The splay faults, one longer back thrust, and two shorter forethrusts, are interpreted from aftershocks (Waldhauser et al., 2012), seafloor observations (Chauhan et al., 2009; Sibuet et al., 2007; Singh et al., 2008), and tsunami modeling (DeDontney & Rice, 2011). The mesh for this model has elements with edge lengths of 1 km along the faults, 4 km at the surface, and 100 km in the volume far from the fault; mesh resolution varies gradually between these conditions. We ensure that the element size along the megathrust and splay faults is sufficient to capture the cohesive zone following the analysis in Wollherr et al. (2018) and detailed in Appendix A.

The regional rock properties are adapted from Laske et al. (2013) and include four layers of oceanic crust and four layers of continental crust with the properties outlined in Table 1. As shown in Figure 1, the layers of oceanic
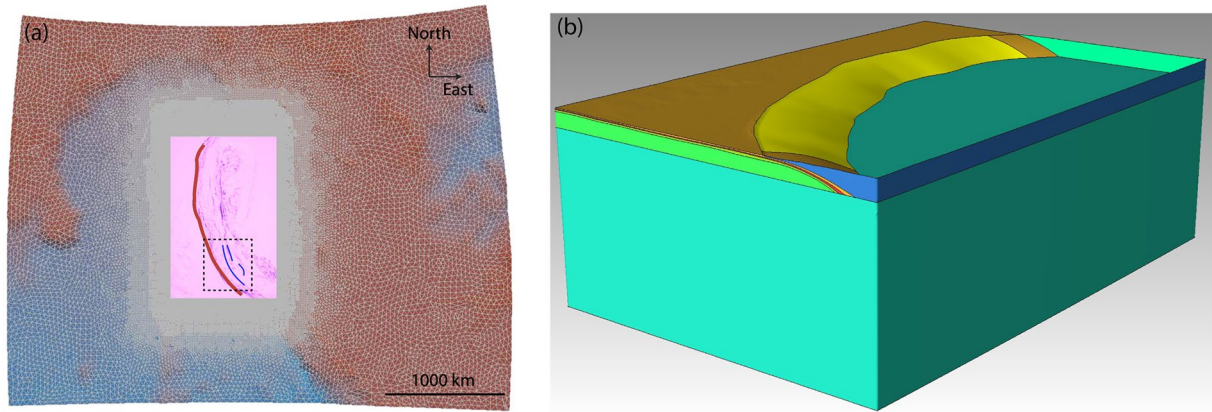
Figure 1. (a) Surface of model demonstrating adaptive meshing in gray. Mesh resolution is finer within the pink box to resolve the topography at the surface and the megathrust and splay faults at depth. Dark red is land and blue is water. Red line is megathrust trace. Dashed black lines highlight the splay fault region and blue lines are the traces of the three splay faults included in model. Figure adapted from Uphoff et al. (2017). Mesh details differ from Uphoff et al. (2017) and are included in Appendix A. (b) Zoom to oblique view of the pink region in (a). Yellow surface is the megathrust, which intersects the seafloor to left and reaches 50 km depth to right. Splays faults not shown, but extend from megathrust to surface. A lower-velocity subduction channel surrounds the megathrust (Table 1). Layers of oceanic crust are horizontal away from the megathrust and curve below it; these are meshed. The continental crust above and right of megathrust is not shown, except by blue border to right. Properties are assigned to layers of continental crust by depth; these layers are not meshed.

crust are horizontal away from the megathrust and curve downward under the megathrust. The continental crust layers are flat everywhere. We assume a linear elastic constitutive law.

3. Model Set-Up and Fault Mechanics

We present six scenarios that all utilize the same structural model based on the 2004 M_w 9.1 Sumatra-Andaman earthquake following Uphoff et al. (2017). The scenarios vary in pre-earthquake pore-fluid pressure (P_f) magnitude and depth gradient, and thus vary in pre-earthquake effective normal stress near the megathrust. In order to isolate the influence of P_f in these scenarios, we choose to scale the megathrust shear traction with the effective normal traction and keep the static and dynamic friction coefficients constant across all scenarios. We step through how these initial conditions are assigned for each scenario in the next subsection, then present the dynamic rupture process and model conditions in the following subsection.

Table 1
Material Properties

Max depth (km)	PV_p (m/s)	V_s (m/s)	ρ (kg/m^3)
Continental crust			
6	6,000	3,500	2,720
12	6,600	3,800	2,860
23	7,100	3,900	3,050
500	8,000	4,450	3,300
Oceanic crust[a]			
6	6,000	3,500	2,720[b]
8	6,600	3,800	2,860
12	7,100	3,900	3,050
30	8,000	4,450	3,300

[a]Max depths are for horizontal layers, away from megathrust. [b]This layer surrounds the megathrust.

3.1. Fluid Pressure, the Regional Stress Field and Fault Tractions

We assume a laterally homogeneous regional stress tensor. Its orientation is from an inversion of focal mechanisms near the hypocenter of the 2004 Sumatra-Andaman earthquake by Karagianni et al. (2015; region 7.1.22). Taking a compression negative sign convention, the maximum compressive stress (σ_3) has an azimuth of 225° and plunges 7°. The intermediate principal stress (σ_2) has an azimuth of 315° and plunges 7°. The least compressive stress (σ_1) has an azimuth of 90° and plunges 80°. In all scenarios, the absolute stresses are proportional to the lithostatic stress ($\sigma_v = \rho g z$, where ρ is the density of rock, g is gravitational acceleration and z is depth) as $\sigma_1 = 0.98\sigma_v$, $\sigma_2 = 1.5\sigma_v$, and $\sigma_3 = 2\sigma_v$. Below 23 km depth, we taper the differential stress to zero at 50 km depth to approximate the transition from brittle to ductile deformation.

We present six scenarios with different P_f magnitudes and depth gradients applied to this absolute stress state (Table 2). Following the effective stress principle (Brace & Kohlstedt, 1980; Hubbert & Rubey, 1959), the effective principal stresses $\left(\sigma_3' < \sigma_2' < \sigma_1'\right)$ for each scenario are determined relative to

Table 2
Initial Conditions for All Scenarios

Scenario	P_f level (% of σ_v [a])	P_f parameterization	Mean τ_s [b] (MPa)	Mean τ_n' [c] (MPa)
1	Low (31%)	$0.31\sigma_v$	101	−506
2	Moderate (62%)	$0.62\sigma_v$	54	−277
3	High (93%)	$0.93\sigma_v$	10	−52
4	Very high (97%)	$0.97\sigma_v$	4	−22
5	High (93%)	σ_v-42 MPa	11	−47
6	Very high (97%)	σ_v-20 MPa	5	−22

Note. Mean values are averaged across the entire fault. Scenarios 1–4 have sublithostatic P_f gradients, while Scenarios 5 and 6 have lithostatic P_f gradients.

[a]Lithostatic (vertical) stress. [b]Initial shear traction. [c]Initial effective normal traction.

the effective lithostatic stress, $\sigma_v' = \sigma_v - P_f$. In Scenarios 1– 4, P_f is applied as a percentage of σ_v, so we refer to this as a sublithostatic P_f gradient.

P_f is hydrostatic in Scenario 1 at 31% of σ_v and moderate in Scenario 2 at 62% of σ_v. High and very high P_f in Scenarios 3 and 4 are set to 93% and 97% of σ_v, respectively. The sublithostatic P_f gradient, the absolute principal stresses and the effective principal stresses are shown for Scenario 4 in Figures 2a–2c.

However, Rice (1992) shows that fluid at elevated pressures within a fault zone may follow the same gradient with depth as σ_v, which causes a constant effective normal stress with depth. We follow this assumption in Scenarios 5 and 6, where high and very high P_f follow the gradient in σ_v, but are offset by constant values (K) of 42 MPa in Scenario 5 and 20 MPa in Scenario 6:

$$P_f = \sigma_v - K \qquad (1)$$

We refer to this as a lithostatic P_f gradient and it is applied below 5 km depth. To resemble borehole stress and fluid-pressure measurements in continental margins (e.g., Suppe, 2014), we apply a lithostatic gradient above 5 km in both scenarios. On average over the rupture area, P_f in Scenarios 5 and 6 is 93% and 97% of σ_v, respectively, mirroring values in Scenarios 3 and 4. The lithostatic P_f gradient, the absolute principal stresses and the effective principal stresses are shown for Scenario 6 in Figures 2d–2f.

In all scenarios, stresses and P_f vary only with depth and do not vary with horizontal location. As P_f increases in these scenarios, the magnitudes of σ_v', σ_3', σ_2' and σ_1' all decrease. In addition, effective normal stress magnitudes (through the effective mean stress) and shear stress magnitudes (through the effective deviatoric stress) decrease as well. Figure 3a shows the relatively low stress magnitudes present at all orientations when a very high P_f magnitude is applied in Scenario 4, while also demonstrating how these stress magnitudes increase with depth in Scenarios 1–4. Figure 3b shows the relatively low stress magnitudes present at all orientations when a very high P_f magnitude is applied in Scenario 6, while also demonstrating how these stress magnitudes are constant with depth in Scenarios 5 and 6.

The initial shear and effective normal tractions, τ_s and τ_n', are determined by projecting the local effective stress tensors onto the non-planar megathrust and splay faults. As for the shear and effective normal stresses, both τ_s and τ_n' magnitudes decrease overall as P_f increases from scenario to scenario. In Scenarios 1–4, τ_s and τ_n' magnitudes increase with depth, while in Scenarios 5 and 6, both are relatively constant with depth. The pre-earthquake tractions are shown for each scenario in Figure 4 and mean values are summarized in Table 2. Setting the effective stress magnitudes relative to σ_v' as we do maintains the same τ_s/τ_n' distribution on the megathrust across all scenarios (Figure B1), which isolates the influence of P_f on earthquake behavior, as desired in this study.

While the on-fault tractions mirror the near-fault stresses in many ways, our 3-D, geometrically complex fault structure comprised of a non-planar megathrust and splay faults modulates the fault traction distributions. As a result, they depart in certain locations from the linear stress gradients and feature additional spatial variations and heterogeneity, as both τ_s and τ_n' vary with fault geometry in all scenarios. Figure B1 illustrates how this distribution varies due to the non-planar megathrust geometry. In Scenarios 5 and 6, where the P_f gradient is lithostatic and τ_s and τ_n' are relatively constant with depth, the variation due to the megathrust geometry is ≈5 MPa.

### 3.2. Failure and Spontaneous Propagation

In all scenarios, dynamic earthquake rupture starts by forced nucleation in the southeastern corner of the megathrust at 30 km depth. Failure occurs when τ_s exceeds the static fault strength, T_{fs}, which is determined from the on-fault frictional cohesion, c, and the product of the coefficient of static friction, μ_s, and τ_n' as (compression is negative):

$$T_{fs} = c - \mu_s \tau_n' \qquad (2)$$
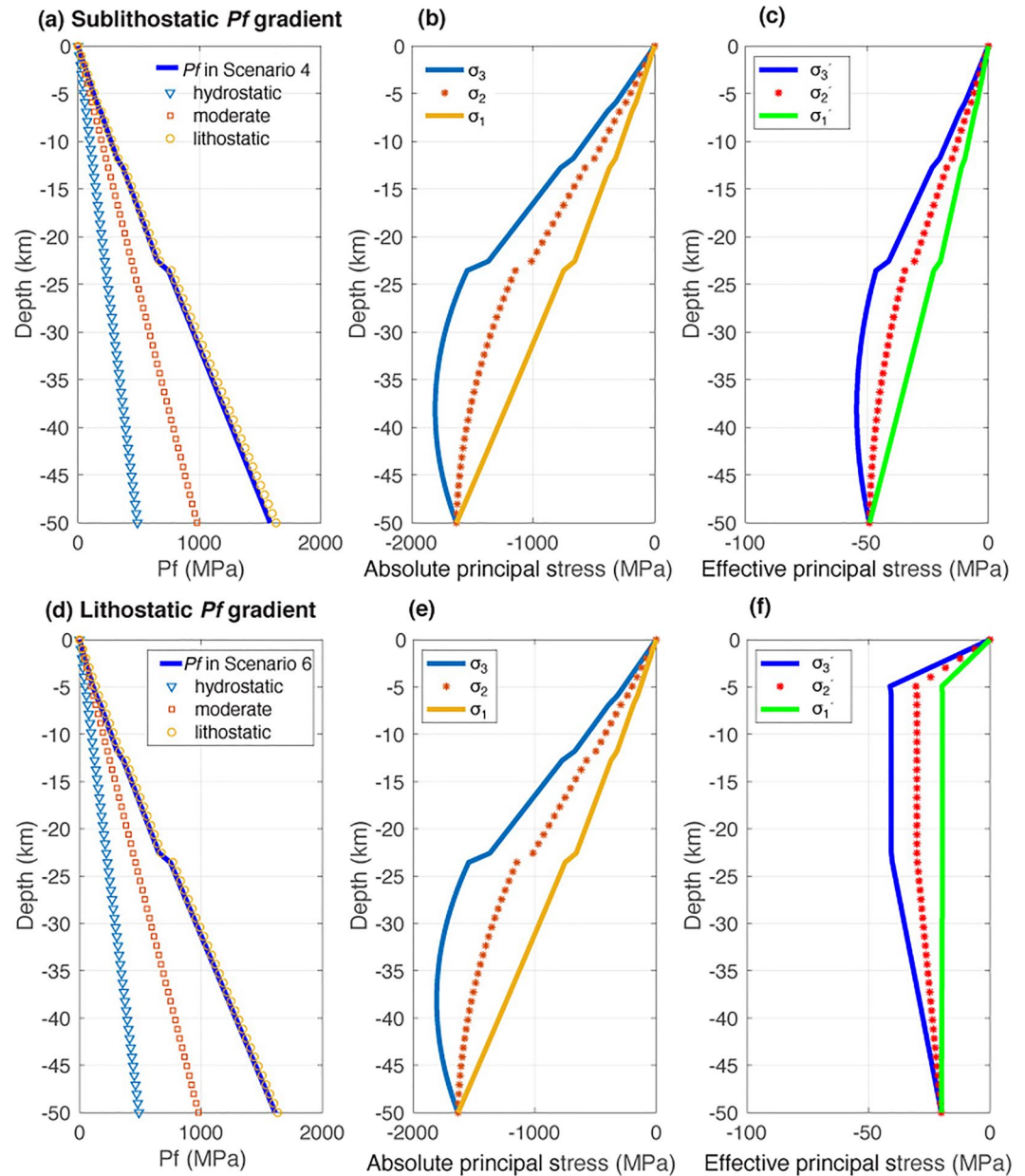
Figure 2. (a) Sublithostatic P_f gradient in Scenario 4 in comparison with hydrostatic, moderate, and lithostatic pressure gradients. (b) The resulting absolute and (c) effective principal stresses for Scenario 4. (d) Lithostatic P_f gradient in Scenario 6 in comparison with hydrostatic, moderate, and lithostatic pressure gradients. (e) The resulting absolute and (f) effective principal stresses for Scenario 6. In all six scenarios, absolute principal stresses have the same depth profiles; magnitudes scale inversely with P_f magnitude (b and e). Whether the P_f gradient is sublithostatic or lithostatic changes the effective principal stress depth profiles; magnitudes scale inversely with P_f magnitude (c and f). Stresses and P_f vary only with depth, not with horizontal location.

c is the frictional strength of a fault in the absence of τ'_n. In situ, c depends on local mineralogy and lithology, but here c is used as a standard proxy for near-surface behavior that we do not model explicitly, mainly the constitutive behavior of shallow sediments in the near-trench region (e.g., Harris et al., 2018; Kaneko et al., 2008). We set $c = 0.4$ MPa along the megathrust and splay faults below 10 km depth, but c linearly increases to 15 MPa from 10 to 0 km depth. Due to topography, the intersection of the fault and the seafloor ranges between 3 and 5 km depth, so maximum c values on the faults at the seafloor range from 8 to 11 MPa. For further discussion of c, please see Section 5.1 and Appendix B.
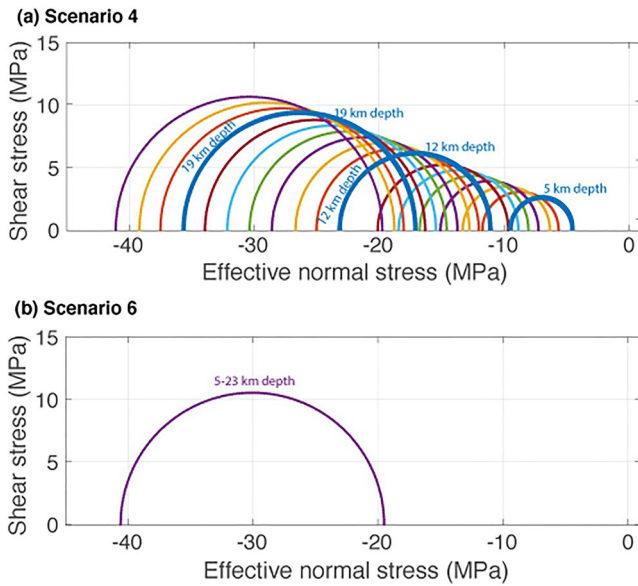
Figure 3. Mohr circles showing shear and effective normal stress at all possible fault orientations from 5 to 23 km depth in (a) Scenario 4 and (b) Scenario 6. As shown for Scenario 4 here, the sublithostatic P_f gradient in Scenarios 1–4 causes the stresses to increase with depth (to the left). Stress magnitude ranges widen progressively from Scenario 3 to Scenario 2 to Scenario 1, but the pattern is the same. As shown for Scenario 6 here, the lithostatic P_f gradient in Scenarios 5 and 6 causes the stresses to be constant with depth. The stress magnitudes are larger in Scenario 5, but remain constant with depth. Below 23 km, the differential stress is tapered to zero in all scenarios (not shown).

We assign $\mu_s = 0.4$ to all faults in all scenarios. Borehole estimates of stress in upper crustal rocks suggest that rocks follow Byerlee's law with $\mu_s = 0.6$–1.0 (Suppe, 2014; Townend & Zoback, 2000, 2004). Our choice of $\mu_s = 0.4$ is motivated by the lithology of the shallow megathrust characterized by high, clay-rich sediment input that is progressively strengthened by dehydration and compaction near the megathrust (Hüpers et al., 2017). Our choice to keep μ_s constant across all faults and all scenarios allows us to here focus on the effects of P_f magnitude and depth gradient.

We apply a linear slip-weakening friction law (e.g., Andrews, 1976) to represent dynamic weakening of a fault after failure. μ_s decreases to the coefficient of dynamic friction, μ_d, over the slip-weakening distance, D_c. After weakening, the dynamic strength of the fault during slip, T_{fd}, is given by:
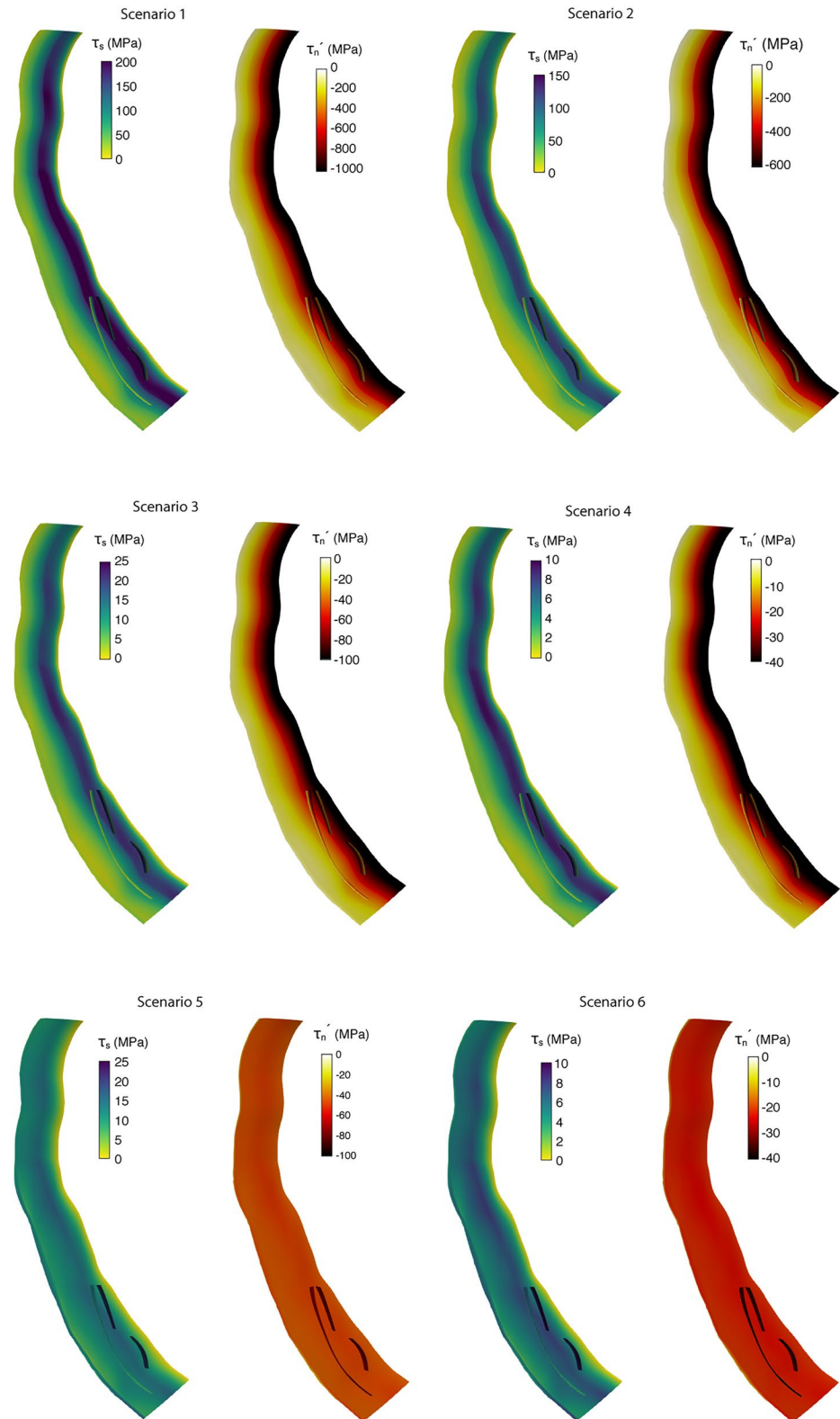
$$T_{fd} = -\mu_d \tau'_n \tag{3}$$

We assign $\mu_d = 0.1$ and use a constant value of $D_c = 0.8$ m. The rupture continues to propagate as long as τ_s locally exceeds T_{fs} and a fault continues to slip as long as sufficient strain energy is available. Note that τ_s at the rupture front is typically higher than the initial τ_s, so statically stronger parts of a fault may fail after the rupture initiates elsewhere.

4. Results

4.1. Earthquake Source Characteristics

Table 3 summarizes average characteristics of the earthquakes in each scenario. As pore fluid pressure (P_f) increases from low to very high, the moment magnitude (M_w) decreases, as do mean cumulative slip, peak slip rate (PSR), mean dynamic stress drop ($\Delta\tau_s$), and rupture velocity (Vr). This reflects our here chosen set-up, in which both shear and effective normal tractions scale inversely with P_f. M_w of the earthquakes in Scenarios 1 and 2 are unrealistically large, which supports the conjecture by Saffer and Tobin (2011) that pore fluid is likely overpressured everywhere along the seismogenic megathrust. Further details about Scenarios 1 and 2 are given in Appendix C. M_w for the earthquakes in Scenarios 3–6 are reasonable for a rupture area the size of the Sumatra earthquake (Strasser et al., 2010), thus, we focus on the results for these four scenarios. Videos of the slip rate evolving along the megathrust during each of these scenarios are available by link from Appendix D.

In all four scenarios, an initially crack-like rupture develops into sharp, boomerang-shaped rupture pulses propagating along-arc on the megathrust. Each pulse consists of multiple rupture fronts, which are caused by reflected waves and head waves generated at structural interfaces and the complex free surface (Huang et al., 2014). We note that pulse-like rupture is here not caused by self-healing due to the dynamics of fault strength (Gabriel et al., 2012), but due to geometric constraints (Weng & Ampuero, 2019). Figure 5 compares slip, PSR, $\Delta\tau_s$, and Vr on the megathrust at the end of the earthquakes in Scenarios 3–6. All three splay faults incorporated into the base model are dynamically activated in all scenarios. In general, they slip an order of magnitude less than the megathrust.

The magnitude of P_f inversely affects average cumulative slip, while its gradient (sublithostatic or lithostatic) influences the slip distribution on the megathrust (Figure 5). As P_f increases from high in Scenario 3 to very high in Scenario 4, mean slip decreases from 26 to 8 m. This is reflected in the decrease in earthquake moment magnitude from M_w 9.3 in Scenario 3 to M_w 9.0 in Scenario 4. The slip is similarly distributed in both scenarios, with maximum slip in the middle of the fault in the downdip direction. Slip is highest in the center of the fault along strike. Likewise, as P_f increases from high in Scenario 5 to very high in Scenario 6, mean slip decreases from 36 to 10 m and moment magnitude decreases from M_w 9.4 to M_w 9.1.

Figure 4. Initial shear traction (τ_s) and effective normal traction (τ_n') on the megathrust in Scenarios 1–6. For each fault image, the shallowest part of the megathrust, near the seafloor, is to the left and the deepest part at 50 km depth is to the right. Note the depth-dependent τ_n' in Scenarios 1–4 with sublithostatic P_f gradients applied vs. the nearly constant τ_n' in Scenarios 5 and 6 with lithostatic P_f gradients. Both τ_s and τ_n' vary with the non-planar fault geometry up to ≈5 MPa.

Table 3
Earthquake Characteristics Averaged Across the Megathrust

Scenario	M_w	Mean slip (m)[a]	Mean PSR (m/s)[b]	Mean $\Delta\tau_s$ (MPa)[c]	Mean Vr (m/s)[d]
1	10.2	470	75	79	4,765
2	9.9	235	46	42	4,246
3	9.3	26	10	8	3,025
4	9.0	8	5	3	2,370
5	9.4	36	11	7	3,203
6	9.1	10	6	3	2,624

[a]Cumulative slip. [b]Peak slip rate. [c]Dynamic stress drop. [d]Rupture velocity.

Mean slip and M_w are similar in scenarios with the same P_f magnitude, but different depth gradients, for example, in Scenarios 3 and 5 and in Scenarios 4 and 6. However, in Scenarios 5 and 6, in which the P_f gradient is lithostatic and effective normal stress is constant with depth, maximum slip is shifted updip relative to the locations of maximum slip in Scenarios 3 and 4, in which the P_f gradient is sublithostatic and constant effective normal stress increases with depth. Slip to the trench only occurs in Scenario 5, and slip is limited at the trench in Scenarios 3, 4, and 6. We discuss this further in Section 5.1 and Appendix E).

As with cumulative slip, peak slip rate PSR in these scenarios decreases as P_f magnitude increases and the P_f gradient influences its distribution along the megathrust. Mean PSR is 10 m/s in Scenario 3 with high P_f and 5 m/s in Scenario 4 with very high P_f. Mean PSR is 11 m/s in Scenario 5 with high P_f and decreases to 6 m/s in Scenario 6 with very high P_f. Comparing across P_f gradients, we see that Scenarios 3 and 5 and Scenarios 4 and 6 have similar mean PSR values, but maximum PSR occurs below 35 km depth in Scenarios 3 and 4 and above 15 km in Scenarios 5 and 6. Thus, relative to depth-dependent effective normal stress under sublithostatic P_f conditions, assuming a lithostatic P_f gradient resulting in constant effective normal stress with depth shifts maximum PSR updip (Figure 5). In addition, more of the megathrust experiences high PSR in Scenario 6 relative to Scenario 4, though maximum values are lower in Scenario 6.

We measure the mean dynamic stress drop ($\Delta\tau_s$) as the average change in shear traction (τ_s) from the initial value to the dynamically reached value at the end of the earthquake. As for mean slip and PSR, P_f has an inverse relationship with mean $\Delta\tau_s$. Mean $\Delta\tau_s$ is 8 MPa in Scenario 3 and 7 MPa in Scenario 5, and 3 MPa in both Scenarios 4 and 6. The distribution of $\Delta\tau_s$ varies with the P_f depth gradient. In Scenarios 3 and 4, $\Delta\tau_s$ is larger along the deeper fault, reaching values of 15 and 7 MPa, respectively, below 30 km depth (Figure 5). In Scenarios 5 and 6, $\Delta\tau_s$ is relatively constant along the central fault in the downdip direction. The highest values are farther updip near 20 km depth, at 12 and 5 MPa in these scenarios, respectively. In all scenarios, $\Delta\tau_s$ is largest along the central portion of the fault along strike.

In contrast to the other earthquake characteristics, there is little variation in the distribution of Vr with P_f depth gradient. However, an increase in P_f magnitude overall causes a decrease in average rupture velocity, Vr, from 3,025 m/s in Scenario 3 to 2,370 m/s in Scenario 4 and from 3,206 m/s in Scenario 5 to 2,624 m/s in Scenario 6. Mean Vr is lower in Scenario 3 relative to Scenario 5, and lower in Scenario 4 relative to Scenario 6, suggesting that average Vr increases under conditions of constant vs. depth-dependent effective normal stress.

In all scenarios, average Vr is sub-Rayleigh relative to the lower velocity subduction channel surrounding the megathrust slip interface (V_s = 3,500 m/s, Table 1). While Vr is below Rayleigh wave speed across most of the megathrust in all scenarios, exceptions of supershear rupture appear (a) propagating updip from the hypocenter at close to P wave speed triggered by energetic nucleation and (b) in the form of localized and relatively slow supershear fronts excited before the sub-Rayleigh rupture front at several isolated locations. In Scenario 5, where Vr is highest out of all scenarios, at these isolated locations $Vr \approx 70\%$ of P wave speed. Vr that exceeds the S wave speed, but remains lower than the P wave speed, agrees with inferences and modeling for earthquake rupture in damaged fault zones (Bao et al., 2019; Harris & Day, 1997; Huang et al., 2016; Oral et al., 2020).

4.2. Post-Earthquake Stress Field

The dynamic rupture model utilized in these scenarios permits investigation of the post-earthquake absolute stress field. We compare principal stress orientations and relative magnitudes along a cross-section of the central part of the rupture in Scenarios 3–6 (see inset in Figure 6a). Figure 6a shows the orientations of the principal stresses ($\sigma_3 < \sigma_2 < \sigma_1$, compression is negative) before the earthquake for all scenarios and Figure 6b shows the orientations after dynamic earthquake rupture in Scenario 4. The post-earthquake stress orientations for Scenarios 3–6 are shown in Figure F1. We summarize the post-earthquake stress orientations for all scenarios in stereonets focused on the hanging wall and footwall regions close to the fault in Figure 6c. We compare the mean
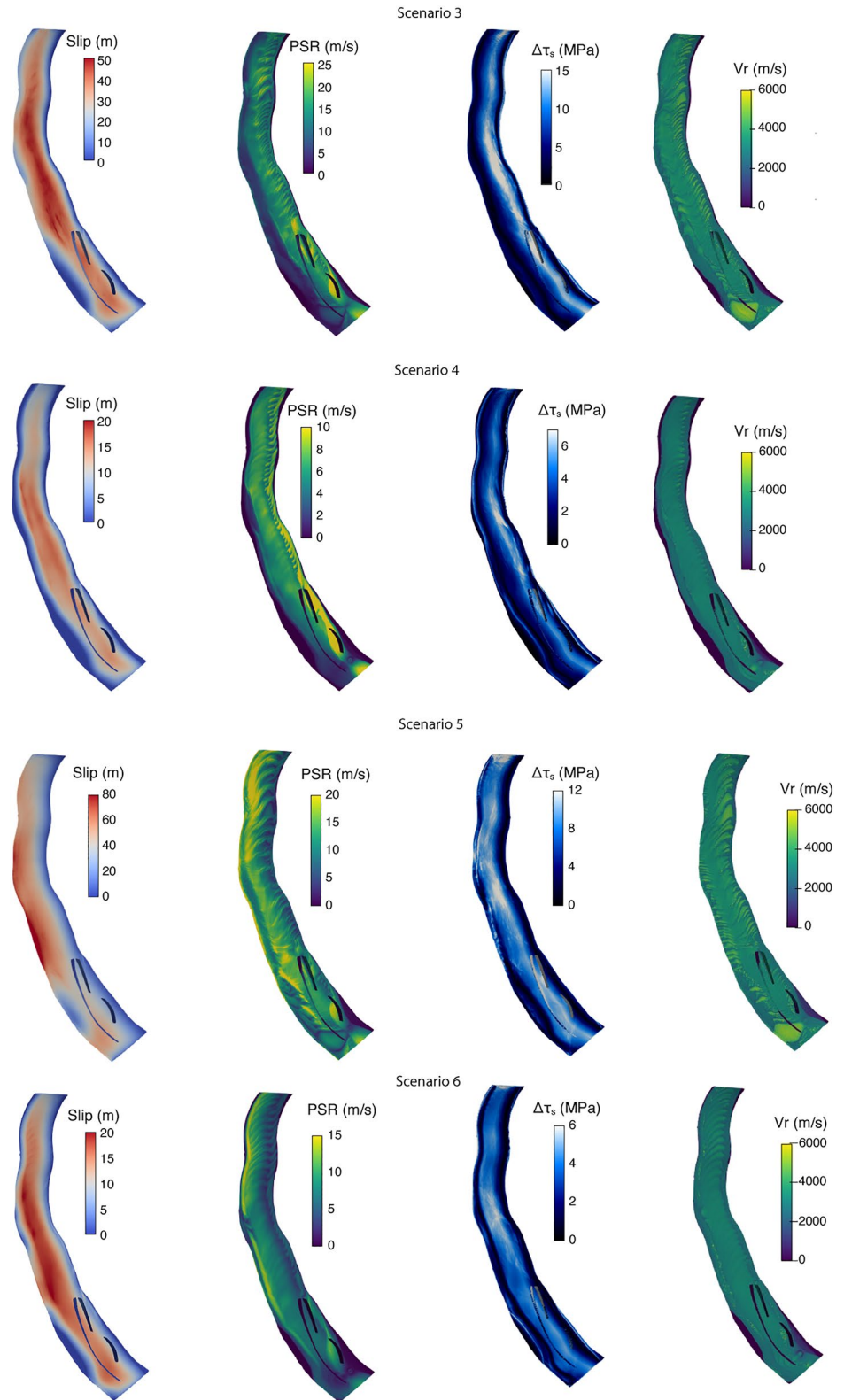
Figure 5. For Scenarios 3–6: cumulative slip, peak slip rate (PSR), dynamic stress drop ($\Delta\tau_s$), and rupture velocity (Vr) on the megathrust. For each fault image, the shallowest part of the fault is to the left and the deepest part (at 50 km depth) is to the right. A version with alternative colorbar limits that are set for comparison across scenarios is included as Figure C2.
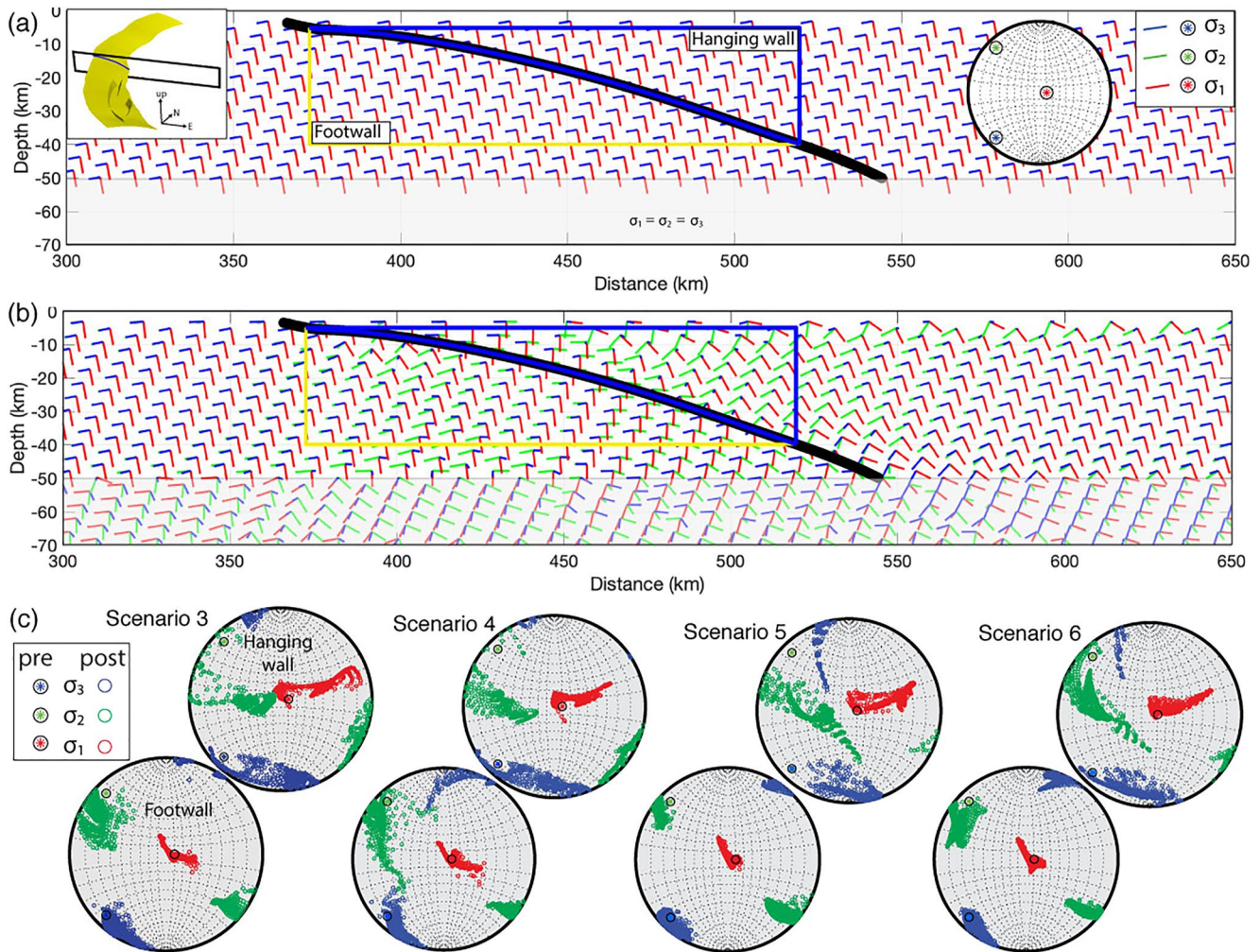
Figure 6. (a) Orientations of the principal stresses before the earthquake for all scenarios. σ_2 vectors are behind σ_3 vectors. The black line is the megathrust profile. Blue and yellow lines outline the hanging wall and footwall regions analyzed in (c). The left inset shows the cross-section location through the model volume near the megathrust (yellow). The right inset shows the stereonet of pre-earthquake principal stresses. (b) Orientations after the dynamic earthquake rupture in Scenario 4, with a sublithostatic P_f gradient. (c) Stereonets of post-earthquake principal stress orientations in Scenario 4. Hanging wall and footwall regions are outlined in (a and b).

orientations of the principal stresses in the hanging wall before and after the earthquake in Table 4 and report average rotations in Table 5. We note that the reported changes in orientation from before to after the earthquake are "apparent" rotations and do not account for a principal stress switching locations with another principal stress

Table 4
Pre- and Post-Earthquake Mean Principal Stress Orientations[a]

Scenario		σ_3 trend	Plunge	σ_2 trend	Plunge	σ_1 trend	Plunge
All	Pre	$225° \pm 0°$	$7° \pm 0°$	$315° \pm 0°$	$7° \pm 0°$	$90° \pm 0°$	$80° \pm 0°$
3	Post	$184° \pm 41°$	$7° \pm 5°$	$258° \pm 56°$	$36° \pm 26°$	$53° \pm 34°$	$51° \pm 24°$
4	Post	$193° \pm 33°$	$7° \pm 5°$	$253° \pm 60°$	$22° \pm 18°$	$48° \pm 37°$	$66° \pm 16°$
5	Post	$197° \pm 64°$	$9° \pm 11°$	$257° \pm 33°$	$44° \pm 20°$	$70° \pm 16°$	$42° \pm 19°$
6	Post	$197° \pm 35°$	$9° \pm 6°$	$277° \pm 40°$	$22° \pm 16°$	$68° \pm 20°$	$64° \pm 16°$

[a]Calculated in vertical slice and in hanging wall only (see Figure 6).

Table 5
Apparent Mean Coseismic Principal Stress Rotations[a]

Scenario	σ_3 rotation	σ_2 rotation	σ_1 rotation
3	46° ± 18°	50° ± 20°	34° ± 20°
4	36° ± 18°	38° ± 18°	21° ± 11°
5	55° ± 16°	58° ± 17°	39° ± 17°
6	36° ± 18°	36° ± 20°	19° ± 14°

[a]Calculated in vertical slice through hanging wall only (see Figure 6).

due to magnitude changes. These apparent rotations are similar to rotations inferred from earthquake data, for which information is available only before and after an earthquake.

In all scenarios, the principal stresses rotate more in the hanging wall than in the footwall. In the hanging wall across all scenarios, the trend of σ_3 rotates counterclockwise by 28°–40° toward parallel with megathrust strike, while its plunge remains shallow at 7°–9°. σ_2 rotates counterclockwise by 38°–63° and its plunge steepens by 15°–37°. σ_1 rotates counterclockwise by 20°–42° and its plunge shallows by 14°–38° from near-vertical (80°) to moderate (42°–66°).

In all scenarios, σ_2 and σ_3 have similar mean apparent rotations and rotate more than the minimum principal stress, σ_1. The mean principal stress rotations in the hanging wall summarized in Table 5 vary with the magnitude of pore fluid pressure (P_f). As P_f increases from Scenario 3 to Scenario 4 and from Scenario 5 to Scenario 6, mean rotations of each principal stress decrease in accordance with decreasing stress drop. Scenarios 4 and 6 have very similar apparent rotations for each principal stress, suggesting that the choice of P_f depth gradient does not affect the amount of rotation when the P_f magnitude is very high (97% of the lithostatic pressure, σ_v). Such similarity is not apparent when comparing Scenarios 3 and 5. Mean rotations in Scenario 5 are the largest of all scenarios, which we attribute to the high fault slip at the trench in this scenario.

To better understand the post-earthquake stress field, we also consider the effective principal stress magnitudes relative to one another. This is important to the stress rotation analysis, because magnitudes of two principal stresses that move closer to one another approach the condition for switching orientations, allowing for a larger amount of heterogeneity in the post-earthquake stress field. Figure 7 shows the maximum differential stress, $\sigma'_{d13} = \sigma'_1 - \sigma'_3$, before and after the dynamic earthquake ruptures in Scenarios 3–6. Prior to each earthquake, the distributions of σ'_{d13} depend on the gradient in P_f. Scenarios 3 and 4 have the same depth-dependent pattern of σ'_{d13}, but the maximum σ'_{d13} values in each scenario differ by up to 30 MPa. Similarly, Scenarios 5 and 6 have the same pattern, with relatively constant values to ~25 km depth (when stress tapering begins), but the maximum σ'_{d13} values in each scenario differ by up to 20 MPa.

Table 6 summarizes the mean values of all three differential stresses in the hanging wall: σ'_{d13}, $\sigma'_{d12} = \sigma'_1 - \sigma'_2$ and $\sigma'_{d23} = \sigma'_2 - \sigma'_3$. As P_f increases from Scenario 3 to Scenario 4 and from Scenario 5 to Scenario 6, pre-earthquake σ'_{d13} averages in the hanging wall decrease by ≈20 MPa. In each scenario, σ'_{d12} equals σ'_{d23} before the earthquake, as σ_2 is initially set to be halfway between σ_3 and σ_1. Pre-earthquake, the magnitudes of these differential stresses differ from Scenario 3 to Scenario 4 and from Scenario 5 to Scenario 6 by ≈10 MPa.
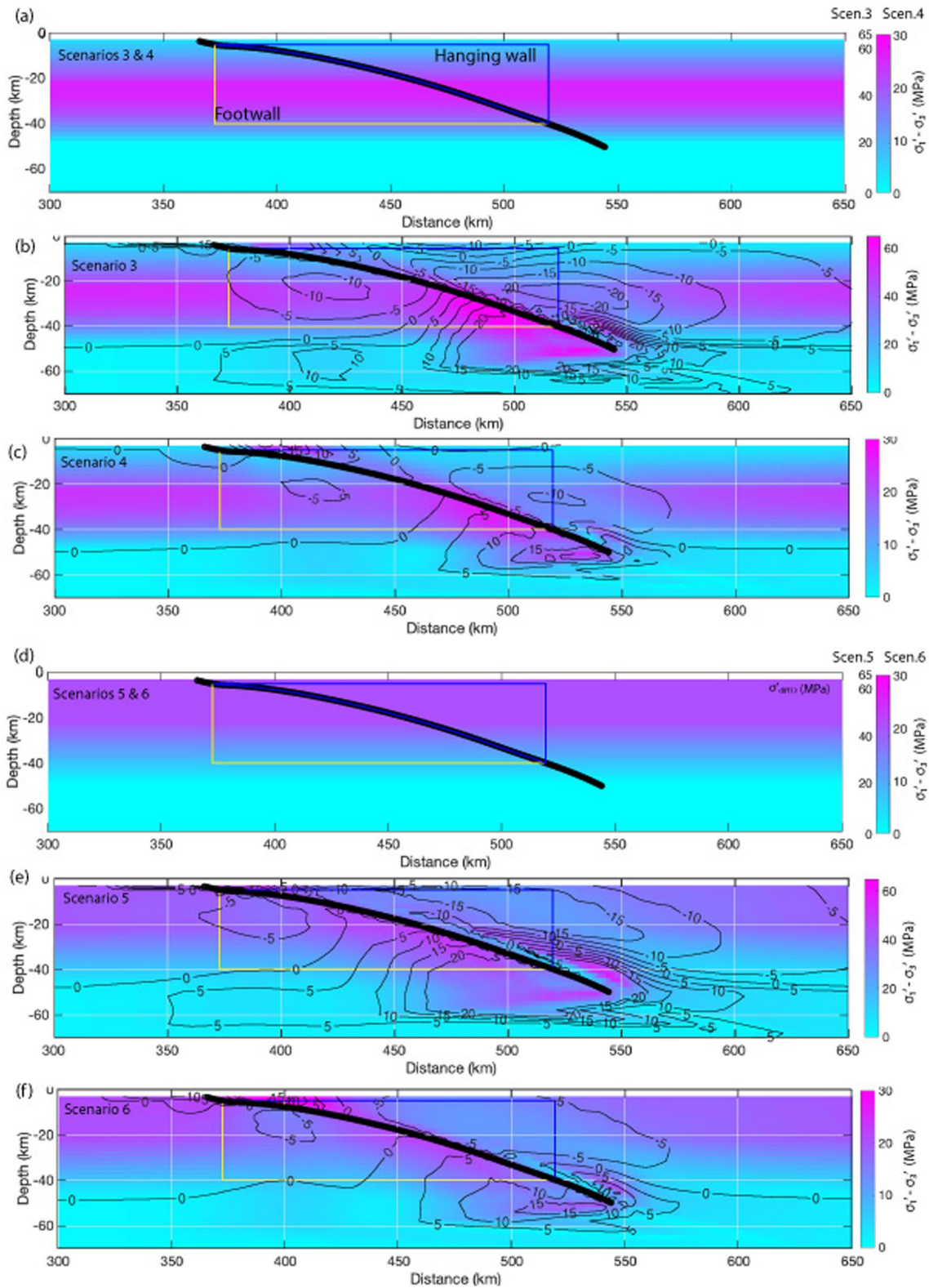
In the plots of the post-earthquake σ'_{d13} distributions in Figure 7, contours indicate the amount and direction (increase or decrease) of the change in σ'_{d13}. σ'_{d13} decreases in the footwall in all scenarios along the central fault, but increases below the bottom of the fault. σ'_{d13} decreases in the hanging wall in all scenarios, except near the end of the fault at depth. Decreases in σ'_{d13} in the hanging wall are larger in Scenarios 3 and 5, reaching 15 MPa and above over larger areas near the megathrust, corresponding to the larger slip in these scenarios relative to Scenarios 4 and 6, respectively. Decreases in σ'_{d13} reach 10 MPa in Scenario 4 and 5 Mpa in Scenario 6.

Table 6
Differential Stress Before and After the Earthquake[a]

Scenario	σ'_{d13} pre[b]	σ'_{d13} post	σ'_{d12} pre	σ'_{d12} post	σ'_{d23} pre	σ'_{d23} post
3	34 ± 14	27 ± 10	17 ± 7	15 ± 7	17 ± 7	12 ± 4
4	15 ± 6	12 ± 5	7 ± 3	7 ± 3	7 ± 3	5 ± 2
5	42 ± 5	31 ± 5	21 ± 3	18 ± 7	21 ± 3	12 ± 5
6	20 ± 2	14 ± 4	10 ± 1	9 ± 2	10 ± 1	5 ± 3

[a]Calculated in vertical slice through hanging wall only (see Figure 6). [b]Maximum differential stress, $\sigma'_{d13} = \sigma'_1 - \sigma'_3$ (MPa).

In all scenarios, there are larger changes in average σ'_{d23} than in average σ'_{d12} due to the larger coseismic decrease in the magnitude of σ'_3 relative to the decreases in σ'_1 and σ'_2 (Table 5). The closeness of σ'_2 and σ'_3 before the earthquake therefore controls the amount of apparent post-seismic stress rotation here, and how likely these two principal stresses are to switch locations. In contrast, σ'_2 and σ'_1 have less apparent rotation, making them less likely to swap orientations.

Figure 7. Cosesimic change in maximum effective differential stress (σ'_{d13}) (a) before the earthquake in Scenarios 3 and 4, (b) after the earthquake in Scenario 3, (c) after the earthquake in Scenario 4, (d) before the earthquake in Scenarios 5 and 6, (e) after the earthquake in Scenario 5, and (f) after the earthquake in Scenario 6. Contours show change in σ'_{d13} from pre-to post-earthquake. Location is as shown in inset in Figure 6.

5. Discussion

We present six earthquake scenarios that vary in P_f magnitude and depth gradient in order to explore the dynamic effects of different pre-earthquake P_f levels and distributions in subduction zones. The model structure and input are consistent with conditions for the 2004 Sumatra-Andaman earthquake, using a base model following (Uphoff et al., 2017). We first discuss how the scenario earthquakes reflect observations of that event, as well as more general observations of earthquakes along megathrusts. Then, we discuss inferences from these scenarios relevant to fault mechanics. We analyze further the stress rotations from before to after these scenario earthquakes and compare them to observations following the 2004 Sumatra earthquake.

5.1. Earthquake Characteristics

Pre-earthquake conditions are not easily constrained by observations, here along the Sumatra-Andaman trench or elsewhere in the world. However, the observational matching of the base model by Uphoff et al. (2017) used here gives an ideal starting point to explore the effects of P_f on earthquake dynamics. In addition, the 3-D physics-based forward modeling approach unifies the pre-earthquake conditions together with the earthquake dynamics to arrive at physically consistent earthquake characteristics, a capability of large-scale and geometrically complex computational models highlighted by Ulrich et al. (2022).

To first order, Scenarios 3 and 6 produce earthquakes with moment magnitudes similar to those inferred for the Sumatra earthquake of M_w 9.1–9.3 (Shearer & Bürgmann, 2010), while the Scenario 4 earthquake is just below this range at M_w 9.0 and the Scenario 5 earthquake is just above this range at M_w 9.4 (Table 3). Maximum slip values from kinematic source inversions compiled by Shearer and Bürgmann (2010) range up to a maximum value of ≈35 m, suggesting that slip in the Scenario 5 earthquake, which averages 36 m, is too large. Seno (2017) estimates a mean stress drop of 3 MPa for this earthquake, which is matched by those for Scenarios 4 and 6. In contrast, Scenarios 3 and 5 have mean dynamic stress drops that are more than twice this value. The mean rupture velocities in Scenarios 4 and 6, respectively 2,370 and 2,624 m/s, are similar to the rupture velocity of 2,500 m/s inferred by Ammon et al. (2005) for the 2004 earthquake. In contrast, Scenarios 3 and 5 both have mean Vr exceeding 3,000 m/s.

Seno (2017) estimates a subducted sediment thickness of 1.57 ± 0.12 km near Simeulue, in the southern region of the 2004 earthquake, which is high in comparison with other subduction zones. Correlation between subducted sediment thickness, stress drop and P_f by Seno (2017) suggests that P_f should be high and stress drop should be low in this earthquake, as in both Scenarios 4 and 6. This highlights the earthquakes in Scenarios 4 and 6 as more realistic.

Scenarios 4 and 6 both have very high P_f at 97% of the lithostatic stress (σ_v), but differ in the way that P_f is acting on the curved fault system. In Scenario 4, P_f follows a sublithostatic depth gradient and the effective normal traction (τ_n') increases with depth. In Scenario 6, following theoretical work by Rice (1992), P_f follows the lithostatic gradient, maintaining a constant difference to σ_v. As a result, τ_n' is close to constant with depth along most of the megathrust (varying only by up to 5 MPa due to variations in fault geometry). The good performances of Scenarios 4 and 6 relative to observations of the 2004 Sumatra earthquake suggest that megathrust earthquakes may occur under very high pre-earthquake P_f magnitudes, resulting in low τ_n' magnitudes. Scenario 6 emerges as the scenario that best matches observations, as Scenario 4 has lower slip that results in a M_w 9.0 event, smaller than the M_w 9.1–9.3 2004 earthquake (Shearer & Bürgmann, 2010). This furth suggests that megathrust earthquakes may occur under conditions of a lithostatic P_f depth gradient, resulting in relatively constant τ_n' along the megathrust.

These scenarios also are representative of variable conditions that may be present along a single megathrust at the same point in time, due to spatial variations in P_f magnitude and/or gradient. Such variations in P_f are one possible mechanism of conceptual seismic asperities, inducing heterogeneity in dynamic fault motion (Bürgmann, 2018; Lay et al., 2012). Sediments and high P_f have been proposed as important mechanisms aiding stable sliding along geometric, frictional and rheological barriers, while (less effectively) thermal pressurization may provide a mechanism for stress-roughening slip events (Barbot, 2019; Gabriel et al., 2020; Perry et al., 2020; Wibberley & Shimamoto, 2005). Our presented scenarios serve as building blocks for future along-arc heterogeneous models that may be calibrated with site-specific friction and pore-fluid measurements to constrain dynamically plausible

megathrust strength and P_f gradients. For example, we find that very high P_f leading to constant effective normal stress with depth produces a stress drop on the megathrust that is nearly constant with depth and pushes PSR updip on the megathrust. Also, earthquake magnitude and mean cumulative slip are larger for an equal or lower mean stress drop under these conditions. For a given subduction zone or megathrust event, such detailed conditions may be constrained by geodetic, geological, or tsunami observations (e.g., Ulrich et al., 2022).

High or very high P_f that follows the lithostatic gradient favors higher slip at shallower depths, thus increasing the importance of near-trench strength and constitutive behavior in determining megathrust hazard. Widespread and high amplitude slip to the trench only occurs in Scenario 5, and slip is limited at the trench in Scenarios 3, 4, and 6. In all scenarios, near-trench behavior is influenced by the choice of on-fault cohesion, c, which is used as a proxy for near-trench behavior that we do not model explicitly here, such as velocity-strengthening during slip in shallow sediments (e.g., Kaneko et al., 2008) and the energy lost to rock yielding around the megathrust (off-fault plasticity, e.g., Gabriel et al., 2013). c is the same in all scenarios, but its relative contribution to the static fault strength increases as the P_f increases and τ_n' magnitude decreases (Equation 2, Figure 4). Models that aim to capture natural co-seismic near-trench processes (e.g., Dunham et al., 2011; Lotto et al., 2019; Ma, 2012; Ma & Nie, 2019; Ulrich et al., 2022) can further discriminate governing factors of near-trench behavior (see also Appendix E). Specifically, Ulrich et al. (2022) focus on near-trench behavior during the 2004 Sumatra earthquake and its influence on the subsequent Indian Ocean tsunami.

Next, we look to general observations of stress drop from earthquakes on the subduction interface to further decipher between scenarios. Allmann and Shearer (2009) report depth-dependent stress drops when data is considered separately by region. Uchide et al. (2014) find an increasing stress drop from 30 to 60 km depth in a spectral decomposition analysis of smaller events occurring before the 2011 Tohoku earthquake. However, Bilek and Lay (2018) and Denolle and Shearer (2016) report very weak correlation between stress drop and depth. Abercrombie et al. (2021) re-evaluate previous studies based on the spectral decomposition method and show that when trade-offs between attenuation and depth-dependent sources are accounted for, the correlation between stress drop and depth from previous studies decreases and, in some cases, disappears altogether. We determine the dynamic stress drop on the megathrust in each scenario, which differs slightly from these observationally inferred values, but remains well within observational and methodological uncertainties. We find that dynamic stress drop varies more with depth in Scenarios 3 and 4 (up to 15 MPa), due to the depth-dependent effective normal traction resulting from the sublithostatic P_f gradient (Figure 5). In contrast, stress drop varies up to only 7 MPa in Scenarios 5 and 6, where effective normal traction is relatively constant along the megathrust resulting from the lithostatic P_f gradient. Thus, a correlation between stress drop and depth is more consistent with high P_f following a sublithostatic gradient, while a low dependence of stress drop on depth is more consistent with high P_f following a lithostatic gradient. Should these end-member conditions be present in different locations along a single megathrust, deciphering a dependence of stress drop on depth observationally will be difficult. On the other hand, well-constrained observations of depth-dependent vs. depth-constant stress drops of small events may differentiate between locations of sublithostatic (e.g., Scenarios 1–4) vs. lithostatic (e.g., Scenarios 5 and 6) P_f gradients along megathrusts.

Under a lithostatic P_f gradient, the effective normal stress is constant and the effective normal tractions (τ_n') are relatively constant, but variations of $\approx$5 MPa still arise due to variations in fault geometry. Bletery et al. (2016) attribute the location and extent of the 2004 Sumatra earthquake rupture to a region of relatively homogeneous megathrust shear strength. Homogeneity of τ_n', and therefore of fault shear strength in these scenarios, is promoted by high P_f that follows the lithostatic gradient with depth. Such homogeneous shear strength is more likely to be exceeded simultaneously over large areas, leading to the large earthquakes observed in subduction zones. However, it is interesting to note that conditions of relatively homogeneous τ_n' and shear strength may actually emphasize the influence of geometry on earthquake behavior, as geometry becomes the main control on shear strength variation along the megathrust. Both effects may be explored in future work focusing on variations in megathrust geometric complexity and cycles of fault slip (e.g., Perez-Silva et al., 2021) and by relaxing our assumption of a constant shear to effective normal traction ratio.

5.2. Inferences From These Scenarios Relevant to Fault Mechanics

Here, we consider the scenarios in light of inferences about fault mechanics, beginning with the initial shear traction (τ_s) on the fault, then discussing effective normal traction (τ'_n) magnitudes and variation with depth. τ_s scales with τ'_n from scenario to scenario and the distribution of τ_s/τ'_n is the same in all scenarios (Figure B1). A static friction coefficient of 0.4 is applied in all scenarios.

From force-balance studies, Lamb (2006) finds that the crust above 7 out of 9 studied subduction zones sustains an average τ_s of 7–15 MPa. This includes Sumatra, with an average τ_s of 15.2 MPa (Lamb, 2006, Table 5), which is similar to the mean τ_s prior to rupture on the megathrust in Scenarios 3 and 5. Brodsky et al. (2020, Figure 6) constrain τ_s on the shallow part of the Tohoku megathrust prior to the 2011 Tohoku earthquake at ≈1.7 MPa using a friction coefficient derived from low-velocity friction experiments. Yao and Yang (2020) find the shear strength of the megathrust that ruptured in the 2012 Nicoya earthquake to be less than 7.5 MPa on average. In combination with observed low-stress drops of subduction megathrust events (Sibson & Rowland, 2003), low dynamic shear stresses during earthquake rupture (e.g., less than 1 MPa, Choy & Boatwright, 1995; Pérez-Campos & Beroza, 2001) also support low τ_s on megathrusts prior to earthquakes, although this may include additional weakening from a variety of dynamic effects (Gao & Wang, 2014).

In this suite of six scenarios, more reasonable earthquakes emerge at higher pre-earthquake P_f magnitudes and average initial τ_s values in Scenarios 3–6 range from 5 to 11 MPa (Table 2). Thus P_f higher than approximately 93% of the lithostatic gradient is consistent with inferences of low initial shear stress on the megathrust. As suggested by the analysis in Section 5.1, Scenarios 4 and 6 produce the most realistic earthquakes, supporting P_f averaging at 97% of the lithostatic stress (σ_v) and consistent with mean τ_s on the megathrust of 4–5 MPa. There are exceptions to inferences of low initial τ_s, however. Lamb (2006) estimates values of 18.3 and 36.7 MPa on the Chile and Tonga megathrusts, respectively, while depth-dependence is inferred for the Tohoku and northern Hikurangi megathrusts with values ranging up to 80 MPa (Gao & Wang, 2014; K. Wang et al., 2019). These values are more consistent with Scenarios 3 and 5.

In all scenarios, the megathrust is moderately strong, with a static friction coefficient of 0.4. However, the low shear strengths (T_{fs}, Equation 2) of the megathrust in the preferred scenarios can be used to classify the megathrust as weak. The megathrust also is dynamically weak, with friction dropping to 0.1 during sliding.

In these scenarios, high P_f magnitude leads to low effective maximum differential stress and low τ_s along the megathrust. However, this can occur independently of P_f, for example, from absolute principal stresses that are close to one another in magnitude. We assume a least compressive principal stress, σ_1, in our scenarios that is close to σ_v. The other two principal stresses must be larger in magnitude in a thrust faulting regime, but are more difficult to constrain. σ_3 could vary from what we choose, which would then change τ_s on the megathrust as well as the average τ_s associated with a particular P_f. More complicated stress conditions also are likely. For example, we choose to set σ_2 midway between σ_1 or σ_3, but this is not necessarily the case in nature. In addition, principal stress magnitudes may vary in magnitude or orientation along the megathrust, both laterally and with depth. Past earthquakes may leave heterogeneous shear tractions on the megathrust and P_f likely varies spatially in the vicinity of the megathrust (Heise et al., 2017). Close to the fault, there is field evidence of stress rotations within the damage zone that vary the principal stress orientations from those in the remote field (Faulkner et al., 2006) and this condition is supported by theory (Rice, 1992). It will be interesting to relate stress complexity with P_f and additional along-arc heterogeneity in future work.

5.3. Off-Fault Results

It has been suggested that principal stress rotations are promoted by complete or near-complete stress drops that permit principal stresses to swap orientations (Brodsky et al., 2020, 2017; X. Wang & Morgan, 2019). However, by connecting 2-D stress rotations to the ratio of stress drop over pre-earthquake deviatoric stress magnitude, Hardebeck (2012, 2015) shows that partial stress release may generate moderate rotations. Scenarios 3 and 5 experience the largest rotations, but have larger initial differential stresses and larger post-earthquake differential stresses as well. The larger rotations in these scenarios appear to scale with fault slip and stress drop, both of which are larger than in Scenarios 4 and 6. X. Wang and Morgan (2019) attribute observed changes in stress orientations following the 2011 Tohoku earthquake to rapid weakening of a statically strong fault with μ_s in the

range of 0.3–0.6. K. Wang et al. (2019) attribute rotations to a weak megathrust, with a low effective friction coefficient (0.032) and low shear stress in the forearc leading to low shear traction on the megathrust. These theories are compatible with one another, if the megathrust is considered to be statically strong, but dynamically weak, in terms of its dynamic friction coefficient, and if P_f is high. This is supported by the scenarios presented here, with $\mu_s = 0.4$ and $\mu_d = 0.1$.

None of the scenarios results in a complete stress drop and yet we find that the postseismic stress field supports a variety of potential aftershock focal mechanisms. In all scenarios, σ_3 rotates toward parallel with megathrust strike and its plunge remains more or less unchanged, while the plunge of σ_2 increases and the plunge of σ_1 decreases. This post-seismic stress state supports a variety of aftershock mechanisms, including strike-slip faulting where σ_1 plunges more shallowly relative to σ_2, and reverse faulting where σ_2 plunges more shallowly relative to σ_1. Of 13 M_w 6 or larger aftershocks with focal mechanisms solutions in the GCMT catalog (Dziewonski et al., 1981; Ekström et al., 2012) occurring along the central rupture within five years of the 2004 Sumatra mainshock (through 27 December 2009), 8 are reverse and 5 are strike-slip. We define the central rupture here as the region from 5° to 9° latitude, 91°–97.3° longitude, and 0–50 km depth, corresponding to the location of the fault-perpendicular slice in Figure 6. Out of 125 M_w 5 or larger aftershocks occurring within 1 month of the mainshock in the same region, 63 have strike-slip focal mechanisms, while 29 have reverse, 31 have normal mechanisms and 2 cannot be categorized.

At Sumatra, Hardebeck (2012) finds rotations of the maximum compressive principal stress, which we call σ_3, relative to the megathrust and in the 2-D plane perpendicular to the megathrust, to be up to ≈42° and increasing from South to North. Along the central rupture (zone B in Hardebeck, 2012), average σ_3 rotation is 26° ± 13°. Using the 2-D solution proposed by Hardebeck and Hauksson (2001), the ratio of the mean earthquake stress drop to the magnitude of the deviatoric stress, $\Delta\tau_s/\sigma_{dev}$, can be estimated as a function of the pre-earthquake angle of σ_3 to the megathrust and its rotation. At Sumatra specifically, Hardebeck (2012) finds that this ratio varies from 0.6 along the southern part of the rupture to 0.8 along the central and northern part of the rupture. This implies that 60%–80% of the pre-earthquake deviatoric stress magnitude along the megathrust was relieved by the earthquake. The apparent rotations of σ_3 along the central rupture in the scenarios presented here (Table 5) are of similar magnitudes to those determined from data (Hardebeck, 2012), ranging from 36° to 55°, but are predominantly in the horizontal plane. We find similar average ratios of $\Delta\tau_s$ to σ_{dev} in these scenarios, of 0.6 in Scenarios 4, 5, and 6 and of 0.7 in Scenario 3, when taking σ_{dev} from these 3-D models as the difference between σ_3 and the mean stress. We do not see correspondence between differences in $\Delta\tau_s/\sigma_{dev}$ and the amount of σ_3 rotation (Table 5), but note that this analysis is not directly comparable to the 2-D analysis by Hardebeck (2012), as σ_3 rotates out of the plane perpendicular to the megathrust in these scenarios.

Post-earthquake stress and aftershock focal mechanism heterogeneity would be further promoted in a model incorporating a heterogeneous initial stress field. In these scenarios, a laterally constant, depth-dependent regional stress tensor is applied, so P_f and the resulting effective stress field are the same near to and far from the megathrust before the earthquake. Such similar on- and off-fault stresses are not likely in nature. Away from the megathrust, secondary faulting, the earthquake history, and material contrasts likely produce stress heterogeneities (van Zelst et al., 2020). Heterogeneity in the magnitude of the effective intermediate principal stress, σ_2', relative to the maximum and minimum effective principal stresses also would contribute to aftershock heterogeneity, by making it easier for different faulting regimes to be activated. For example, as we note in Section 4.2, the magnitude of σ_2' relative to the other two effective principal stresses controls the ability for σ_2' to switch places with σ_1' or σ_3', thus affecting postseismic stress rotations. In addition, dynamic effects that decouple conditions on- and off-fault, such as thermal pressurization (Noda, 2008; Noda et al., 2009) during which P_f increases rapidly due to reduced pore pressure diffusion in the fault zone during slip, may allow low effective normal tractions on the megathrust, even while a different stress state persists away from the fault. Considering more complex initial stress conditions off the fault and decoupling on- and off-fault stresses are clear next steps for this work.

6. Conclusions

We analyze the effects of pore fluid pressure (P_f) magnitude and gradient on pre-earthquake stress conditions and earthquake dynamics using 3-D high-performance computing enabled, physics-based dynamic rupture models that permit geometrically complex faults. The six scenarios presented, based on the 2004 M_w 9.1 Sumatra-Andaman

earthquake, have P_f that varies from hydrostatic to lithostatic under sublithostatic vs. lithostatic gradients. These result, respectively, in either depth-dependent or constant effective normal stress near the megathrust and splay faults. As P_f increases in these scenarios, moment magnitude, cumulative slip, peak slip rate, dynamic stress drop, and rupture velocity all decrease. A lithostatic P_f gradient causes relatively constant effective normal tractions on the megathrust, moves peak slip and peak slip rate updip, and produces a more constant stress drop across the megathrust. This is consistent with theoretical analysis and observations inferring that the stress drops of smaller earthquakes in subduction zones are only weakly depth-dependent.

In comparison with a range of observations, we identify two preferred scenarios that both support the presence of very high coseismic P_f on average over the ruptured area (here 97% of the lithostatic pressure). These have low mean shear and effective normal traction magnitudes of 4–5 and 22 MPa, respectively. The mean dynamic stress drop for these two scenario earthquakes is 3 MPa and the mean rupture velocity is 2,400–2,600 m/s, similar to observations of the 2004 Sumatra-Andaman earthquake. Although comparison with observations of the 2004 earthquake cannot conclusively differentiate between these two preferred scenarios, a lithostatic P_f gradient, which causes constant normal stress near the megathrust, may be the theoretically more plausible condition under very high P_f magnitudes. On weak megathrusts, in terms of low static shear strength and low dynamic friction during rupture, where P_f follows the lithostatic gradient, near-trench strength and constitutive behavior are crucially important for megathrust hazard, as peak slip and peak slip rate occur at shallower depths.

Mean apparent rotations of the principal stresses in the hanging wall decrease as P_f magnitude increases, but do not vary with P_f gradient. Scenarios with the largest rotations have larger initial differential stress and larger post-earthquake differential stress as well. The larger rotations in these scenarios scale with fault slip and stress drop. Along the central rupture, maximum compressive stress rotations in the hanging wall average $36° \pm 18°$ toward trench-parallel in the two preferred scenarios and the minimum principal stress rotates from near-vertical toward a shallower plunge. This post-earthquake stress field is consistent with the heterogeneous aftershocks observed following the Sumatra earthquake.

Variations in P_f are one possible mechanism of conceptual seismic asperities, and our analysis may serve as guidance for future along-arc heterogeneous models. In addition, this work has implications for tsunami hazard, as the P_f gradient is shown to influence the location of maximum slip and slip rate. Under conditions of a lithostatic P_f gradient, relatively constant effective normal tractions downdip along the megathrust push maximum slip and slip rate toward the surface.

Appendix A: Model Mesh Resolution

Dynamic rupture simulations must resolve the cohesive zone width Λ, which spans the part of the fault across which shear stress decreases from its static to its dynamic value. In heterogeneous dynamic rupture simulations, Λ can vary considerably across the fault in dependence on initial stress, frictional properties, and propagation distance. Since Λ also changes dynamically across the fault, the number of elements per median Λ can also vary significantly across the fault for a given simulation. Selected findings from Wollherr et al. (2018) allow for a better understanding of how the numerical accuracy of SeisSol's ADER-DG scheme, in resolving on fault time-dependent parameters, is affected by mesh size and polynomial degree. By comparing the rupture arrival time, peak slip rate (PSR) time, final slip and the PSR averaged across 363 receivers with respect to a reference solution, Wollherr et al. (2018) show that errors are globally decreasing with mesh refinement and increasing polynomial degree. SeisSol resolves shear and normal stress and effective friction according to a friction law everywhere at the fault at $(p + 2)^2$ Gaussian quadrature points inside each fault element triangle, with p being the polynomial degree (and $p = 3$ in this study leading to fourth order accuracy in space and time, as measured in the L2 norm, of the ADER-DG scheme for seismic wave propagation).

In this study, we ensure that we resolve the median Λ, estimated at 1 km for Scenario 3, 1.6 km for Scenario 4, 0.9 km for Scenario 5, and 1.5 km for Scenario 6. In assessing sufficient resolution, we follow Day et al. (2005) and Wollherr et al. (2018). Day et al. (2005) define a dynamic rupture solution to be sufficiently close to the reference solution once the RMS errors reached the following thresholds: lower than 0.2% for rupture arrival time, lower than 7% for PSR and lower than 1% for final slip. We calculate Λ as the difference in distance between the rupture front arrival time and the first point in time at which shear stresses reach their dynamic value across the

fault. The minimum Λ (approximated at the fifteenth percentile of all measured) varies across the scenarios as follows: 346 m in Scenario 3, 540 m in Scenario 4, 469 m in Scenario 5 and 627 m in Scenario 6. By analyzing Scenarios 3 and 6, with the longest and shortest Λ, we find that the errors for rupture arrival range from 0.09% to 0.20% and for final slip range from 0.68% to 1.2% across these four scenarios, which are sufficiently small with respect to the findings by Day et al. (2005). The expected errors for PSR are higher, ranging from 8.9% to 17%, above the 7% recommended by Day et al. (2005), however, Ramos et al. (2021) verify with higher resolution models that even with expected errors above 7% for PSR, megathrust slip is not affected in comparable SeisSol dynamic rupture models.

Appendix B: Prestress Ratio and On-Fault Frictional Cohesion

The relative prestress ratio, R, is the ratio of the fault stress drop $(\tau_s - T_{fd})$ to the breakdown strength drop $(T_{fs} - T_{fd})$, where τ_s is the initial shear traction, T_{fs} is the static fault strength and T_{fd} is the dynamic fault strength during sliding (Aochi & Madariaga, 2003). R varies along the megathrust with the non-planar fault geometry (Figure B1), but is nearly the same across all scenarios since τ_s/τ_n' is constant across all scenarios. The exception to this is with respect to the on-fault frictional cohesion, c. c is similar across all scenarios, but contributes differently to T_{fs} in each scenario and these changes R slightly from scenario to scenario, particularly at shallow depths (see also Appendix E).

Cohesion, c, depends on local mineralogy and lithology. However, c is used here to limit slip in the absence of near-trench behavior, using the lowest value that restricts unrealistic slip and rupture dynamics (e.g., occurrence of supershear rupture) at the trench. We find this to be $c = 0.4$ MPa below 10 km depth and increasing linearly to 15 MPa at 0 km depth (Figure B2). We tested two alternative c gradients from 0.4 MPa below 10 km to maxima of 1 and 10 MPa at $z = 0$, which lead to unrealistic near-surface behavior. As the base model used here does not capture the constitutive behavior of shallow sediments in the near-trench region, we do not draw conclusions about near-trench behavior or about realistic c values from these scenarios (see also Appendix E). Ulrich et al. (2022) take the work in this direction by incorporating slip-strengthening behavior near the seafloor, as well as off-fault plasticity, into models of the 2004 Sumatra-Andaman earthquake.
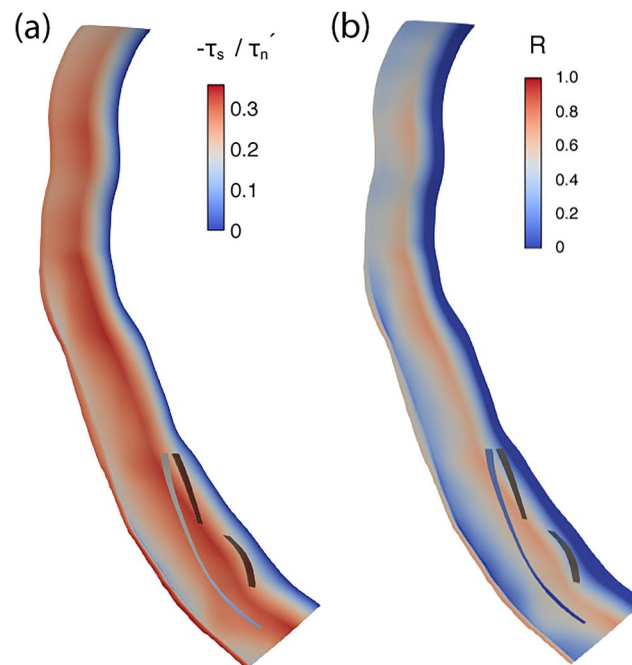
Figure B1. (a) The ratio of the initial shear traction to effective normal traction (τ_s/τ_n') varies depending on the megathrust orientation relative to the local stress tensor, but the distribution on the megathrust is the same across all scenarios. (b) The prestress ratio, R, is shown here for Scenario 4, but is similar in all scenarios.
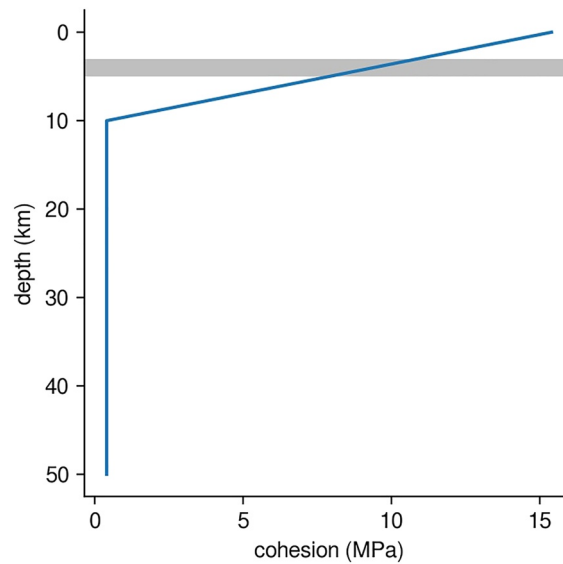
Figure B2. Blue line is on-fault frictional cohesion, c, which is set to 0.4 MPa below 10 km depth and increases linearly to 15 MPa at 0 km depth. Due to topography, the intersection of the fault and the seafloor ranges between 3 and 5 km depth, so maximum c values on the megathrust and splay faults at the seafloor range from 8 to 11 MPa. The gray line shows this intersection between fault and seafloor on average.

When the fault is in tension and effective normal stress equals zero, the fault strength is equal to c. This is because tensile stresses are treated in SeisSol to prevent fault opening following a standard approach in the dynamic rupture community (Harris et al., 2018, 2009). This procedure treats tension on the fault the same as if the effective normal stress equals zero.

Appendix C: Scenarios 1 and 2 Earthquakes

Slip, peak slip rate, dynamic stress drop, and rupture velocity are shown in Figure C1 for Scenarios 1 and 2, which have low and moderate P_f, respectively.
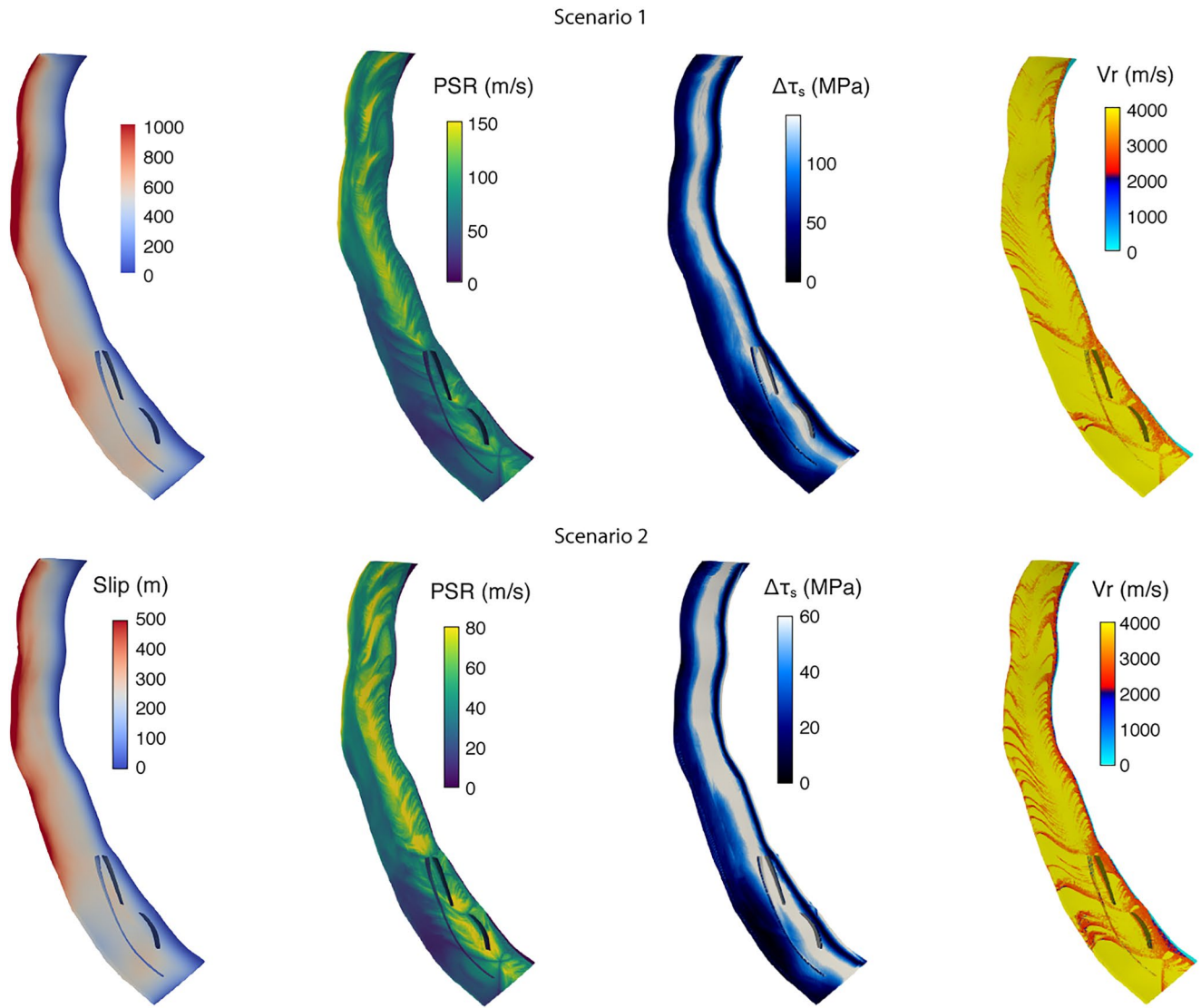
Figure C1. Cumulative slip, peak slip rate (PSR), stress drop ($\Delta\tau_s$), and rupture velocity (*Vr*) on the megathrust in Scenarios 1 and 2. For each fault image, the shallowest part of the fault (where it intersects the seafloor) is to the left and the deepest part (at 50 km depth) is to the right.
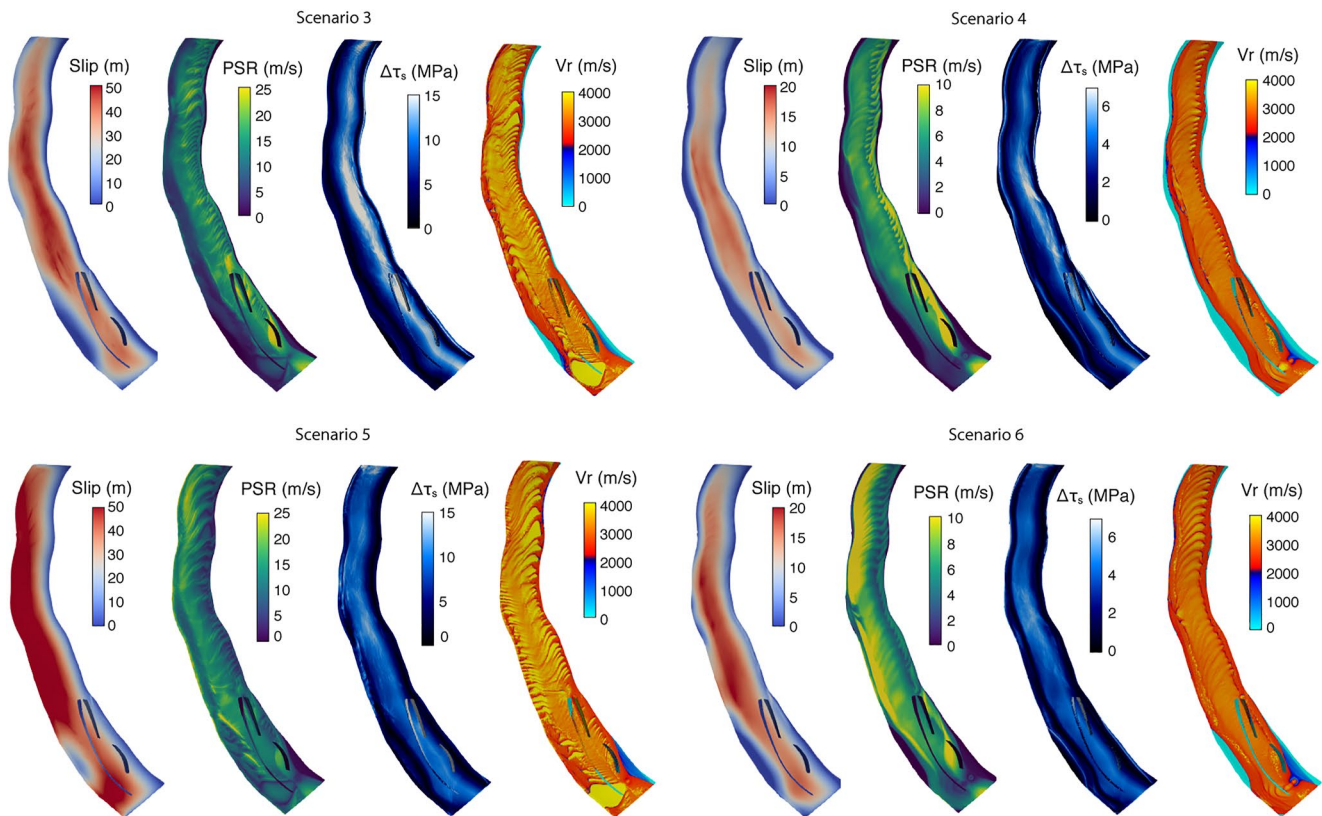
Figure C2. Cumulative slip, peak slip rate (PSR), stress drop ($\Delta\tau_s$), and rupture velocity (Vr) on the megathrust for Scenarios 3–6 with alternative colorbars from Figure 5 that are better for comparison across scenarios. For each fault image, the shallowest part of the fault is to the left and the deepest part (at 50 km depth) is to the right.

Appendix D: Earthquake Videos

We provide animations showing absolute slip rate evolving along the megathrust during the earthquakes in Scenarios 3–6 here: https://doi.org/10.5281/zenodo.5914960.

Appendix E: Slip at the Trench

Slip proceeds to the trench in Scenario 5 and reaches maximum values there, which is clearly different from Scenarios 3, 4, and 6 (Figure 5 and Figure C2). A similar difference between shallow slip in Scenario 4 and Scenario 6 also is visible in Figure 5. These differences are due not only to P_f magnitude and depth gradient, but also to the contribution of the applied on-fault cohesion, c, to static fault strength, T_{fs} (see also Appendix B). In all scenarios, c is constant below 10 km depth and linearly increases toward the surface above, contributing to T_{fs} according to Equation 2. The influence of c on T_{fs} increases as P_f increases and the magnitude of τ'_n decreases. As a result, closeness to failure varies near the seafloor in all scenarios. Fault strength is overcome at the trench only in Scenario 5, while slip is restricted along the top of the fault in Scenarios 3, 4, and 6. This contrast is important because it highlights both that the influence of c on slip behavior at the trench increases as P_f increases and c becomes a larger component of T_{fs}, and that near-trench slip is encouraged by very high P_f following a lithostatic gradient that causes conditions of constant τ'_n along the megathrust and pushes maximum slip and slip rate closer to the trench. In these scenarios, c is defined as the strength of the fault in the absence of τ_n (Equation 2) and is used as a proxy for near-trench behavior that we do not model explicitly here, including the energy lost to damage around the megathrust (off-fault plasticity, e.g., Gabriel et al., 2013) and velocity-strengthening of the fault in shallow sediments (e.g., Kaneko et al., 2008). Further study of slip behavior at the trench requires that the appropriate physical processes near the seafloor are incorporated into the model (e.g., Dunham et al., 2011; Lotto et al., 2019; Ma, 2012; Ma & Nie, 2019; Ulrich et al., 2022). For example, Ulrich et al. (2022) incorporate

slip strengthening and off-fault plasticity of lithified shallow sediments into coupled earthquake-tsunami models of the 2004 Sumatra earthquake and Indian Ocean tsunami to study near-trench slip, seafloor displacement, and tsunami genesis using a coupled tsunami model.

Appendix F: Post-Earthquake Stress Field

Figure F1 shows the post-seismic stress field for all scenarios. While the rotation directions are similar in all scenarios, the amount of rotation is larger in Scenarios 3 and 5 than in Scenarios 4 and 6. Stereonets are included in the main text (Figure 6).
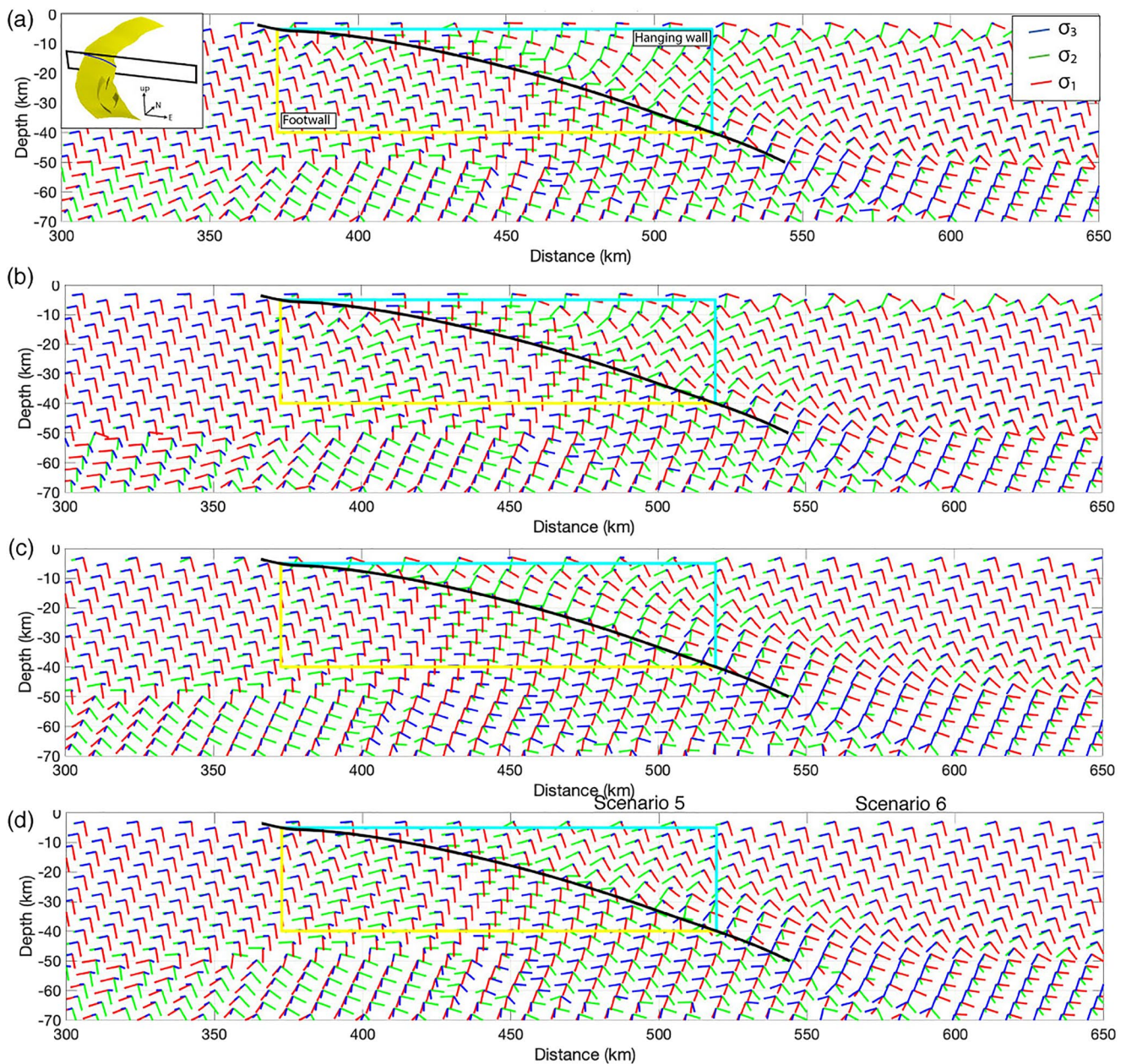
Figure F1. Orientations of the principal stresses after the earthquake in (a) Scenario 3, (b) Scenario 4, (c) Scenario 5 and, (d) Scenario 6. Black line is the megathrust profile. Blue and yellow lines outline the hanging wall and footwall regions. Black box in left inset in (a) shows location of slice through the volume along the fault (yellow).

Data Availability Statement

Simulations were conducted using the open-source software package SeisSol (https://doi.org/10.5281/zenodo.4899349), which also is freely available at https://github.com/SeisSol/SeisSol. All simulation input files are accessible at the Zenodo data repository: https://doi.org/10.5281/zenodo.5914661.

References

Abercrombie, R. E., Trugman, D. T., Shearer, P. M., Chen, X., Zhang, J., Pennington, C., et al. (2021). Does earthquake stress drop increase with depth in the crust? *Earth and Space Science Open Archive*, *41*. https://doi.org/10.1002/essoar.10506989.1

Allmann, B. P., & Shearer, P. M. (2009). Global variations of stress drop for moderate to large earthquakes. *Journal of Geophysical Research: Solid Earth*, *114*(1). https://doi.org/10.1029/2008JB005821

Ammon, C. J., Ji, C., Thio, H.-K., Robinson, D., Ni, S., Hjorleifsdottir, V., et al. (2005). Rupture process of the 2004 Sumatra-Andaman earthquake. *Science*, *308*(5725), 1133–1139. https://doi.org/10.1126/science.1112260

Andrews, D. J. (1976). Rupture propagation with finite stress in antiplane strain. *Journal of Geophysical Research*, *81*(20), 3575–3582. https://doi.org/10.1029/JB081i020p03575

Aochi, H., & Madariaga, R. (2003). The 1999 Izmit, Turkey, earthquake: Nonplanar fault structure, dynamic rupture process, and strong ground motion. *Bulletin of the Seismological Society of America*, *93*(3), 1249–1266. https://doi.org/10.1785/0120020167

Aochi, H., Poisson, B., Toussaint, R., Rachez, X., & Schmittbuhl, J. (2014). Self-induced seismicity due to fluid circulation along faults. *Geophysical Journal International*, *196*(3), 1544–1563. https://doi.org/10.1093/gji/ggt356

Audet, P., Bostock, M. G., Christensen, N. I., & Peacock, S. M. (2009). Seismic evidence for overpressured subducted oceanic crust and megathrust fault sealing. *Nature*, *457*(7225), 76–78. https://doi.org/10.1038/nature07650

Audet, P., & Schwartz, S. Y. (2013). Hydrologic control of forearc strength and seismicity in the Costa Rican subduction zone. *Nature Geoscience*, *6*(10), 852–855. https://doi.org/10.1038/ngeo1927

Bao, H., Ampuero, J.-P., Meng, L., Fielding, E. J., Liang, C., Milliner, C. W., et al. (2019). Early and persistent supershear rupture of the 2018 magnitude 7.5 Palu earthquake. *Nature Geoscience*, *12*(3), 200–205. https://doi.org/10.1038/s41561-018-0297-z

Barbot, S. (2019). Slow-slip, slow earthquakes, period-two cycles, full and partial ruptures, and deterministic chaos in a single asperity fault. *Tectonophysics*, *768*, 228171. https://doi.org/10.1016/j.tecto.2019.228171

Beeler, N. M., Thomas, A., Bürgmann, R., & Shelly, D. (2013). Inferring fault rheology from low-frequency earthquakes on the San Andreas. *Journal of Geophysical Research: Solid Earth*, *118*(11), 5976–5990. https://doi.org/10.1002/2013JB010118

Bilek, S. L., & Lay, T. (2018). Subduction zone megathrust earthquakes. *Geosphere*, *14*(4), 1468–1500. https://doi.org/10.1130/GES01608.1

Bletery, Q., Thomas, A. M., Rempel, A. W., Karlstrom, L., Sladen, A., & De Barros, L. (2016). Mega-earthquakes rupture flat megathrusts. *Science*, *354*(6315), 1027–1031. https://doi.org/10.1126/science.aag0482

Brace, W. F., & Kohlstedt, D. L. (1980). Limits on lithospheric stress imposed by laboratory experiments. *Journal of Geophysical Research: Solid Earth*, *85*(B11), 6248–6252. https://doi.org/10.1029/jb085ib11p06248

Breuer, A., Heinecke, A., & Bader, M. (2016). Petascale local time stepping for the ADER-DG finite element method. In *Proceedings—2016 IEEE 30th International Parallel and Distributed Processing Symposium (IPDPS)* (pp. 854–863). Institute of Electrical and Electronics Engineers Inc. https://doi.org/10.1109/IPDPS.2016.109

Breuer, A., Heinecke, A., Rettenberger, S., Bader, M., Gabriel, A. A., & Pelties, C. (2014). Sustained petascale performance of seismic simulations with SeisSol on SuperMUC. In J. M.Kunkel, T.Ludwig, & H. W.Meuer (Eds.), *Lecture Notes in Computer Science (Including Subseries Lecture Notes in Artificial Intelligence and Lecture Notes in Bioinformatics)* (LNCS, Vol. 8488, pp. 1–18). Springer. https://doi.org/10.1007/978-3-319-07518-1_1

Brodsky, E. E., Mori, J. J., Anderson, L., Chester, F. M., Conin, M., Dunham, E. M., et al. (2020). The state of stress on the fault before, during, and after a major earthquake. *Annual Review of Earth and Planetary Sciences*, *48*(1), 1–26. https://doi.org/10.1146/annurev-earth-053018-060507

Brodsky, E. E., Saffer, D., Fulton, P., Chester, F., Conin, M., Huffman, K., et al. (2017). The post-earthquake stress state on the Tohoku megathrust as constrained by reanalysis of the JFAST breakout data. *Geophysical Research Letters*, *44*(16), 8294–8302. https://doi.org/10.1002/2017GL074027

Bürgmann, R. (2018). The geophysics, geology, and mechanics of slow fault slip. *Earth and Planetary Science Letters*, *495*, 112–134. https://doi.org/10.1016/j.epsl.2018.04.062

Calahorrano, A., Sallarès, V., Collot, J.-Y., Sage, F., & Ranero, C. R. (2008). Nonlinear variations of the physical properties along the southern Ecuador subduction channel: Results from depth-migrated seismic data. *Earth and Planetary Science Letters*, *267*(3), 453–467. https://doi.org/10.1016/j.epsl.2007.11.061

Chauhan, A. P. S., Singh, S. C., Hananto, N. D., Carton, H., Klingelhoefer, F., Dessa, J.-X., et al. (2009). Seismic imaging of forearc back thrusts at northern Sumatra subduction zone. *Geophysical Journal International*, *179*(3), 1772–1780. https://doi.org/10.1111/j.1365-246X.2009.04378.x

Choy, G. L., & Boatwright, J. L. (1995). Global patterns of radiated seismic energy and apparent stress. *Journal of Geophysical Research: Solid Earth*, *100*(B9), 18205–18228. https://doi.org/10.1029/95JB01969

Cruz-Atienza, V. M., Villafuerte, C., & Bhat, H. S. (2018). Rapid tremor migration and pore-pressure waves in subduction zones. *Nature Communications*, *9*(1), 1–13. https://doi.org/10.1038/s41467-018-05150-3

Day, S. M., Dalguer, L. A., Lapusta, N., & Liu, Y. (2005). Comparison of finite difference and boundary integral solutions to three-dimensional spontaneous rupture. *Journal of Geophysical Research: Solid Earth*, *110*(12), 1–23. https://doi.org/10.1029/2005JB003813

DeDontney, N., & Rice, J. R. (2011). Tsunami wave analysis and possibility of splay ault rupture during the 2004 Indian Ocean earthquake. *Pure and Applied Geophysics*, *169*(10), 1707–1735. https://doi.org/10.1007/s00024-011-0438-4

De La Puente, J., Ampuero, J. P., & Käser, M. (2009). Dynamic rupture modeling on unstructured meshes using a discontinuous Galerkin method. *Journal of Geophysical Research: Solid Earth*, *114*(10). https://doi.org/10.1029/2008JB006271

Denolle, M. A., & Shearer, P. M. (2016). New perspectives on self-similarity for shallow thrust earthquakes. *Journal of Geophysical Research: Solid Earth*, *121*(9), 6533–6565. https://doi.org/10.1002/2016JB013105

Dumbser, M., & Käser, M. (2006). An arbitrary high-order discontinuous Galerkin method for elastic waves on unstructured meshes—II. The three-dimensional isotropic case. *Geophysical Journal International*, *167*(1), 319–336. https://doi.org/10.1111/j.1365-246X.2006.03120.x

Dunham, E. M., Belanger, D., Cong, L., & Kozdon, J. E. (2011). Earthquake ruptures with strongly rate-weakening friction and off-fault plasticity, part 2: Nonplanar faults. *Bulletin of the Seismological Society of America*, *101*(5), 2308–2322. https://doi.org/10.1785/0120100076

Dziewonski, A. M., Chou, T.-A., & Woodhouse, J. H. (1981). Determination of earthquake source parameters from waveform data for studies of global and regional seismicity. *Journal of Geophysical Research: Solid Earth*, *86*(B4), 2825–2852. https://doi.org/10.1029/JB086iB04p02825

Eberhart-Phillips, D., Han, D. H., & Zoback, M. D. (1989). Empirical relationships among seismic velocity, effective pressure, porosity, and clay content in sandstone. *Geophysics*, *54*(1), 82–89. https://doi.org/10.1190/1.1442580

Ekström, G., Nettles, M., & Dziewoński, A. M. (2012). The global CMT project 2004–2010: Centroid-moment tensors for 13,017 earthquakes. *Physics of the Earth and Planetary Interiors*, *200–201*, 1–9. https://doi.org/10.1016/j.pepi.2012.04.002

Faulkner, D. R., Mitchell, T. M., Healy, D., & Heap, M. J. (2006). Slip on "weak" faults by the rotation of regional stress in the fracture damage zone. *Nature*, *444*(7121), 922–925. https://doi.org/10.1038/nature05353

Gabriel, A.-A., Ampuero, J.-P., Dalguer, L. A., & Mai, P. M. (2012). The transition of dynamic rupture styles in elastic media under velocity-weakening friction. *Journal of Geophysical Research: Solid Earth*, *117*(B9). https://doi.org/10.1029/2012JB009468

Gabriel, A.-A., Ampuero, J.-P., Dalguer, L. A., & Mai, P. M. (2013). Source properties of dynamic rupture pulses with off-fault plasticity. *Journal of Geophysical Research: Solid Earth*, *118*(8), 4117–4126. https://doi.org/10.1002/jgrb.50213

Gabriel, A.-A., Vyas, J. C., Ulrich, T., Ampuero, J., & Mai, P. M. (2020). 3-D dynamic rupture modeling with thermal pressurization. In *Poster #158 at 2020 SCEC Annual Meeting* (p. 8).

Gao, X., & Wang, K. (2014). Strength of stick-slip and creeping subduction megathrusts from heat flow observations. *Science*, *345*(6200), 1038–1041. https://doi.org/10.1126/science.1255487

Gao, X., & Wang, K. (2017). Rheological separation of the megathrust seismogenic zone and episodic tremor and slip. *Nature*, *543*(7645), 416–419. https://doi.org/10.1038/nature21389

Garagash, D. I. (2012). Seismic and aseismic slip pulses driven by thermal pressurization of pore fluid. *Journal of Geophysical Research: Solid Earth*, *117*(4), https://doi.org/10.1029/2011JB008889

Hardebeck, J. L. (2012). Coseismic and postseismic stress rotations due to great subduction zone earthquakes. *Geophysical Research Letters*, *39*(21), https://doi.org/10.1029/2012GL053438

Hardebeck, J. L. (2015). Stress orientations in subduction zones and the strength of subduction megathrust faults. *Science*, *349*(6253), 1213–1216. https://doi.org/10.1126/science.aac5625

Hardebeck, J. L., & Hauksson, E. (2001). Crustal stress field in southern California and its implications for fault mechanics. *Journal of Geophysical Research*, *106*(B10), 21859–21882. https://doi.org/10.1029/2001jb000292

Harris, R. A., Barall, M., Aagaard, B., Ma, S., Roten, D., Olsen, K., et al. (2018). A suite of exercises for verifying dynamic earthquake rupture codes. *Seismological Research Letters*, *89*(3), 1146–1162. https://doi.org/10.1785/0220170222

Harris, R. A., Barall, M., Archuleta, R., Dunham, E., Aagaard, B., Ampuero, J. P., et al. (2009). The SCEC/USGS dynamic earthquake rupture code verification exercise. *Seismological Research Letters*, *80*(1), 119–126. https://doi.org/10.1785/gssrl.80.1.119

Harris, R. A., & Day, S. M. (1997). Effects of a low-velocity zone on a dynamic rupture. *Bulletin of the Seismological Society of America*, *87*(5), 1267–1280.

Hayes, G. P., Wald, D. J., & Johnson, R. L. (2012). Slab1.0: A three-dimensional model of global subduction zone geometries. *Journal of Geophysical Research*, *117*(B1), B01302. https://doi.org/10.1029/2011JB008524

Heinecke, A., Breuer, A., Rettenberger, S., Bader, M., Gabriel, A. A., Pelties, C., et al. (2014). Petascale high order dynamic rupture earthquake simulations on heterogeneous supercomputers. In *SC '14: Proceedings of the International Conference for High Performance Computing, Networking, Storage and Analysis* (Vol. 2015, pp. 3–14). https://doi.org/10.1109/SC.2014.6

Heise, W., Caldwell, T. G., Bannister, S., Bertrand, E. A., Ogawa, Y., Bennie, S. L., & Ichihara, H. (2017). Mapping subduction interface coupling using magnetotellurics: Hikurangi margin, New Zealand. *Geophysical Research Letters*, *44*(18), 9261–9266. https://doi.org/10.1002/2017GL074641

Heise, W., Caldwell, T. G., Bertrand, E. A., Hill, G. J., Bennie, S. L., & Ogawa, Y. (2013). Changes in electrical resistivity track changes in tectonic plate coupling. *Geophysical Research Letters*, *40*(19), 5029–5033. https://doi.org/10.1002/grl.50959

Houston, H. (2015). Low friction and fault weakening revealed by rising sensitivity of tremor to tidal stress. *Nature Geoscience*, *8*(5), 409–415. https://doi.org/10.1038/ngeo2419

Huang, Y., Ampuero, J.-P., & Helmberger, D. V. (2014). Earthquake ruptures modulated by waves in damaged fault zones. *Journal of Geophysical Research: Solid Earth*, *119*(4), 3133–3154. https://doi.org/10.1002/2013JB010724

Huang, Y., Ampuero, J.-P., & Helmberger, D. V. (2016). The potential for supershear earthquakes in damaged fault zones-theory and observations. *Earth and Planetary Science Letters*, *433*, 109–115. https://doi.org/10.1016/j.epsl.2015.10.046

Hubbert, M. K., & Rubey, W. W. (1959). Role of fluid pressure in mechanics of overthrust faulting I. Mechanics of fluid-filled porous solids and its application to overthrust faulting. *GSA Bulletin*, *70*(2), 115–166. https://doi.org/10.1130/0016-7606(1959)70[115:ROFPIM]2.0.CO;2

Hüpers, A., Torres, M. E., Owari, S., McNeill, L. C., Dugan, B., Henstock, T. J., et al. (2017). Release of mineral-bound water prior to subduction tied to shallow seismogenic slip off Sumatra. *Science*, *356*(6340), 841–844. https://doi.org/10.1126/science.aal3429

Husen, S., & Kissling, E. (2002). Postseismic fluid flow after the large subduction earthquake of Antofagasta, Chile. *Geology*, *29*(9), 847–850. https://doi.org/10.1029/2001gl014045

Kaneko, Y., Lapusta, N., & Ampuero, J.-P. (2008). Spectral element modeling of spontaneous earthquake rupture on rate and state faults: Effect of velocity-strengthening friction at shallow depths. *Journal of Geophysical Research: Solid Earth*, *113*(B9). https://doi.org/10.1029/2007JB005553

Karagianni, I., Papazachos, C. B., Scordilis, E. M., & Karakaisis, G. F. (2015). Reviewing the active stress field in Central Asia by using a modified stress tensor approach. *Journal of Seismology*, *19*(2), 541–565. https://doi.org/10.1007/s10950-015-9481-4

Kozdon, J. E., & Dunham, E. M. (2013). Rupture to the Trench: Dynamic rupture simulations of the 11 March 2011 Tohoku earthquake. *Bulletin of the Seismological Society of America*, *103*(2B), 1275–1289. https://doi.org/10.1785/0120120136

Krenz, L., Uphoff, C., Ulrich, T., Gabriel, A.-A., Abrahams, L. S., Dunham, E. M., & Bader, M. (2021). *3-D acoustic-elastic coupling with gravity: The dynamics of the 2018 Palu, Sulawesi earthquake and tsunami*. arXiv:2107.06640 [physics]. (arXiv: 2107.06640).

Lamb, S. (2006). Shear stresses on megathrusts: Implications for mountain building behind subduction zones. *Journal of Geophysical Research*, *111*(B7). https://doi.org/10.1029/2005jb003916

Laske, G., Masters, G., Ma, Z., & Pasyanos, M. (2013). Update on CRUST1.0—A 1° global model of Earth's crust. In *EGU General Assembly 2013* (Vol. 15, p. 2658).

Lay, T., Kanamori, H., Ammon, C. J., Koper, K. D., Hutko, A. R., Ye, L., et al. (2012). Depth-varying rupture properties of subduction zone megathrust faults. *Journal of Geophysical Research: Solid Earth*, *117*(4), 4311. https://doi.org/10.1029/2011JB009133

Liu, Y., & Rice, J. R. (2005). Aseismic slip transients emerge spontaneously in three-dimensional rate and state modeling of subduction earthquake sequences. *Journal of Geophysical Research: Solid Earth*, *110*(8), 1–14. https://doi.org/10.1029/2004JB003424

Liu, Y., & Rice, J. R. (2007). Spontaneous and triggered aseismic deformation transients in a subduction fault model. *Journal of Geophysical Research: Solid Earth*, *112*(9), B09404. https://doi.org/10.1029/2007JB004930

Lotto, G. C., Jeppson, T. N., & Dunham, E. M. (2019). Fully coupled simulations of megathrust earthquakes and tsunamis in the Japan Trench, Nankai Trough, and Cascadia subduction zone. *Pure and Applied Geophysics*, *176*(9), 4009–4041. https://doi.org/10.1007/s00024-018-1990-y

Ma, S. (2012). A self-consistent mechanism for slow dynamic deformation and tsunami generation for earthquakes in the shallow subduction zone. *Geophysical Research Letters*, *39*(11), https://doi.org/10.1029/2012GL051854

Ma, S., & Nie, S. (2019). Dynamic wedge failure and along-arc variations of tsunamigenesis in the Japan Trench margin. *Geophysical Research Letters*, *46*(15), 8782–8790. https://doi.org/10.1029/2019GL083148

Madden, E. H., Bader, M., Behrens, J., Van Dinther, Y., Gabriel, A. A., Rannabauer, L., et al. (2021). Linked 3-D modeling of megathrust earthquake-tsunami events: From subduction to tsunami run up. *Geophysical Journal International*, *224*(1), 487–516. https://doi.org/10.1093/gji/ggaa484

Madden, E. H., Maerten, F., & Pollard, D. D. (2013). Mechanics of nonplanar faults at extensional steps with application to the 1992 *M* 7.3 Landers, California, earthquake. *Journal of Geophysical Research: Solid Earth*, *118*(6), 3249–3263. https://doi.org/10.1002/jgrb.50237

Madden, E. H., & Pollard, D. D. (2012). Integration of surface slip and aftershocks to constrain the 3-D structure of faults involved in the *M* 7.3 landers earthquake, Southern California. *Bulletin of the Seismological Society of America*, *102*(1), 321–342. https://doi.org/10.1785/0120110073

Noda, H. (2008). Frictional constitutive law at intermediate slip rates accounting for flash heating and thermally activated slip process. *Journal of Geophysical Research: Solid Earth*, *113*(9), B09302. https://doi.org/10.1029/2007JB005406

Noda, H., Dunham, E. M., & Rice, J. R. (2009). Earthquake ruptures with thermal weakening and the operation of major faults at low overall stress levels. *Journal of Geophysical Research: Solid Earth*, *114*(7), B07302. https://doi.org/10.1029/2008JB006143

Oeser, J., Bunge, H. P., & Mohr, M., (2006). Cluster design in the Earth Sciences TETHYS. In *Lecture Notes in Computer Science (Including Subseries Lecture Notes in Artificial Intelligence and Lecture Notes in Bioinformatics)*.(LNCS, Vol. 4208, pp. 31–40). Springer Verlag. https://doi.org/10.1007/11847366_4

Oral, E., Weng, H., & Ampuero, J. P. (2020). Does a damaged-fault zone mitigate the near-field impact of supershear earthquakes? Application to the 2018 7.5 Palu, Indonesia, earthquake. *Geophysical Research Letters*, *47*(1), e2019GL085649. https://doi.org/10.1029/2019GL085649

Pelties, C., De La Puente, J., Ampuero, J. P., Brietzke, G. B., & Käser, M. (2012). Three-dimensional dynamic rupture simulation with a high-order discontinuous Galerkin method on unstructured tetrahedral meshes. *Journal of Geophysical Research: Solid Earth*, *117*(2), https://doi.org/10.1029/2011JB008857

Pelties, C., Gabriel, A. A., & Ampuero, J. P. (2014). Verification of an ADER-DG method for complex dynamic rupture problems. *Geoscientific Model Development*, *7*(3), 847–866. https://doi.org/10.5194/gmd-7-847-2014

Pérez-Campos, X., & Beroza, G. C. (2001). An apparent mechanism dependence of radiated seismic energy. *Journal of Geophysical Research: Solid Earth*, *106*(B6), 11127–11136. https://doi.org/10.1029/2000JB900455

Perez-Silva, A., Li, D., Gabriel, A.-A., & Kaneko, Y. (2021). *3-D modeling of long-term slow slip events along the flat slab segment in the Guerrero Seismic Gap*.

Perry, S. M., Lambert, V., & Lapusta, N. (2020). Nearly magnitude-invariant stress drops in simulated crack-like earthquake sequences on rate-and-state faults with thermal pressurization of pore fluids. *Journal of Geophysical Research: Solid Earth*, *125*(3), e2019JB018597. https://doi.org/10.1029/2019JB018597

Petrini, C., Gerya, T., Yarushina, V., van Dinther, Y., Connolly, J., & Madonna, C. (2020). Seismo-hydro-mechanical modeling of the seismic cycle: Methodology and implications for subduction zone seismicity. *Tectonophysics*, *791*, 228504. https://doi.org/10.1016/j.tecto.2020.228504

Ramos, M. D., & Huang, Y. (2019). How the transition region along the Cascadia megathrust influences coseismic behavior: Insights from 2-D dynamic rupture simulations. *Geophysical Research Letters*, *46*(4), 1973–1983. https://doi.org/10.1029/2018GL080812

Ramos, M. D., Huang, Y., Ulrich, T., Li, D., Gabriel, A.-A., & Thomas, A. M. (2021). Assessing margin-wide rupture behaviors along the Cascadia megathrust with 3-D dynamic rupture simulations. *Journal of Geophysical Research: Solid Earth*, *126*(7), e2021JB022005. https://doi.org/10.1029/2021JB022005

Rettenberger, S., Meister, O., Bader, M., & Gabriel, A.-A. (2016). ASAGI: A parallel server for adaptive geoinformation. In *Proceedings of the Exascale Applications and Software Conference 2016* (pp. 1–9). ACM. https://doi.org/10.1145/2938615.2938618

Rice, J. R. (1992). Fault stress states, pore pressure distributions and the weakening of the San Andreas fault, in Fault Mechanics and the Transport Properties of Rocks: A Festschrift in Honor of W …. *Fault Mechanics and Transport Properties of Rocks* (January 1992).

Rice, J. R. (2006). Heating and weakening of faults during earthquake slip. *Journal of Geophysical Research: Solid Earth*, *111*(5). https://doi.org/10.1029/2005JB004006

Rowe, C. D., Meneghini, F., & Moore, J. C. (2009). Fluid-rich damage zone of an ancient out-of-sequence thrust, Kodiak Islands, Alaska. *Tectonics*, *28*(1). https://doi.org/10.1029/2007TC002126

Saffer, D. M. (2017). Mapping fluids to subduction megathrust locking and slip behavior. *Geophysical Research Letters*, *44*(18), 9337–9340. https://doi.org/10.1002/2017GL075381

Saffer, D. M., & Tobin, H. J. (2011). Hydrogeology and mechanics of subduction zone forearcs: Fluid flow and pore pressure. *Annual Review of Earth and Planetary Sciences*, *39*(1), 157–186. https://doi.org/10.1146/annurev-earth-040610-133408

Schmitt, S. V., Segall, P., & Matsuzawa, T. (2011). Shear heating-induced thermal pressurization during earthquake nucleation. *Journal of Geophysical Research: Solid Earth*, *116*(6), B06308. https://doi.org/10.1029/2010JB008035

Segall, P., & Bradley, A. M. (2012). Slow-slip evolves into megathrust earthquakes in 2-D numerical simulations. *Geophysical Research Letters*, *39*(17), 18308. https://doi.org/10.1029/2012GL052811

Segall, P., & Rice, J. R. (1995). Dilatancy, compaction, and slip instability of a fluid-infiltrated fault. *Journal of Geophysical Research*, *100*(B11), 22155–22171. https://doi.org/10.1029/95jb02403

Seno, T. (2017). Subducted sediment thickness and M_w 9 earthquakes. *Journal of Geophysical Research: Solid Earth*, *122*(1), 470–491. https://doi.org/10.1002/2016JB013048

Shearer, P., & Bürgmann, R. (2010). Lessons learned from the 2004 Sumatra-Andaman megathrust rupture. *Annual Review of Earth and Planetary Sciences*, *38*, 103–131. https://doi.org/10.1146/annurev-earth-040809-152537

Shelly, D. R., Beroza, G. C., & Ide, S. (2007). Non-volcanic tremor and low-frequency earthquake swarms. *Nature*, *446*(7133), 305–307. https://doi.org/10.1038/nature05666

Shelly, D. R., Beroza, G. C., Ide, S., & Nakamula, S. (2006). Low-frequency earthquakes in Shikoku, Japan, and their relationship to episodic tremor and slip. *Nature*, *442*(7099), 188–191. https://doi.org/10.1038/nature04931

Sibson, R. H. (1992). Implications of fault-valve behavior for rupture nucleation and recurrence. *Tectonophysics*, *211*(1–4), 283–293. https://doi.org/10.1016/0040-1951(92)90065-E

Sibson, R. H. (1994). Crustal stress, faulting and fluid flow. *Geological Society Special Publication*, *78*(1), 69–84. https://doi.org/10.1144/GSL.SP.1994.078.01.07

Sibson, R. H., & Rowland, J. V. (2003). Stress, fluid pressure and structural permeability in seismogenic crust, North Island, New Zealand. *Geophysical Journal International*, *154*(2), 584–594. https://doi.org/10.1046/j.1365-246X.2003.01965.x

Sibuet, J., Rangin, C., Lepichon, X., Singh, S., Cattaneo, A., Graindorge, D., et al. (2007). 26 December 2004 great Sumatra-Andaman earthquake: Co-seismic and post-seismic motions in northern Sumatra. *Earth and Planetary Science Letters*, *263*(1–2), 88–103. https://doi.org/10.1016/j.epsl.2007.09.005

Singh, S. C., Carton, H., Tapponnier, P., Hananto, N. D., Chauhan, A. P., Hartoyo, D., et al. (2008). Seismic evidence for broken oceanic crust in the 2004 Sumatra earthquake epicentral region. *Nature Geoscience*, *1*(11), 777–781. https://doi.org/10.1038/ngeo336

Strasser, F. O., Arango, M., & Bommer, J. J. (2010). Scaling of the source dimensions of interface and intraslab subduction-zone earthquakes with moment magnitude. *Seismological Research Letters*, *81*(6), 941–950. https://doi.org/10.1785/gssrl.81.6.941

Suppe, J. (2014). Fluid overpressures and strength of the sedimentary upper crust. *Journal of Structural Geology*, *69*(Part B), 481–492. https://doi.org/10.1016/j.jsg.2014.07.009

Tarling, M. S., Smith, S. A., & Scott, J. M. (2019). Fluid overpressure from chemical reactions in serpentinite within the source region of deep episodic tremor. *Nature Geoscience*, *12*(12), 1034–1042. https://doi.org/10.1038/s41561-019-0470-z

Tobin, H. J., & Saffer, D. M. (2009). Elevated fluid pressure and extreme mechanical weakness of a plate boundary thrust, Nankai Trough subduction zone. *Geology*, *37*(8), 679–682. https://doi.org/10.1130/G25752A.1

Tonegawa, T., Kimura, T., Shiraishi, K., Yabe, S., Fukao, Y., Araki, E., et al. (2021). Weak faults at megathrust plate boundary respond to tidal stress. *Earth, Planets, and Space*, *73*(1), 89. https://doi.org/10.1186/s40623-021-01414-3

Townend, J., & Zoback, M. D. (2000). How faulting keeps the crust strong. *Geology*, *28*(5), 399–402. https://doi.org/10.1130/0091-7613(2000)028<0399:hfktcs>2.3.co;2

Townend, J., & Zoback, M. D. (2004). Regional tectonic stress near the San Andreas fault in central and southern California. *Geophysical Research Letters*, *31*(15), 1–5. https://doi.org/10.1029/2003GL018918

Uchide, T., Shearer, P. M., & Imanishi, K. (2014). Stress drop variations among small earthquakes before the 2011 Tohoku-oki, Japan, earthquake and implications for the main shock. *Journal of Geophysical Research: Solid Earth*, *119*(9), 7164–7174. https://doi.org/10.1002/2014JB010943

Ulrich, T., Gabriel, A. A., Ampuero, J. P., & Xu, W. (2019a). Dynamic viability of the 2016 M_w 7.8 Kaikōura earthquake cascade on weak crustal faults. *Nature Communications*, *10*(1), 1213. https://doi.org/10.1038/s41467-019-09125-w

Ulrich, T., Gabriel, A.-A., & Madden, E. H. (2022). Stress, rigidity, and sediment strength control megathrust earthquake and tsunami dynamics. *Nature Geoscience*, *15*(1), 67–73. https://doi.org/10.1038/s41561-021-00863-5

Ulrich, T., Vater, S., Madden, E. H., Behrens, J., van Dinther, Y., van Zelst, I., et al. (2019b). Coupled, physics-based modeling reveals earthquake displacements are critical to the 2018 Palu, Sulawesi tsunami. *Pure and Applied Geophysics*, *176*(10), 4069–4109. https://doi.org/10.1007/s00024-019-02290-5

Uphoff, C., Rettenberger, S., Bader, M., Madden, E., Ulrich, T., Wollherr, S., & Gabriel, A.-A. (2017). Extreme scale multi-physics simulations of the tsunamigenic 2004 Sumatra megathrust earthquake. In SC Proceedings of the International Conference for High Performance Computing, Networking, Storage and Analysis. *Proceedings of the International Conference for High Performance Computing, Networking, Storage, and Analysis*. https://doi.org/10.1145/3126908.3126948

van Zelst, I., Rannabauer, L., Gabriel, A.-A., & Dinther, Y. V. (2020). Earthquake rupture on multiple splay faults and its effect on tsunamis. *EarthArXiv*, *1–20*.

van Zelst, I., Wollherr, S., Gabriel, A., Madden, E. H., & Dinther, Y. (2019). Modeling megathrust earthquakes across scales: One-way coupling from geodynamics and seismic cycles to dynamic rupture. *Journal of Geophysical Research: Solid Earth*, *124*(11), 11414–11446. https://doi.org/10.1029/2019JB017539

Waldhauser, F., Schaff, D. P., Diehl, T., & Engdahl, E. R. (2012). Splay faults imaged by fluid-driven aftershocks of the 2004 M_w 9.2 Sumatra-Andaman earthquake. *Geology*, *40*(3), 243–246. https://doi.org/10.1130/G32420.1

Wang, K., Brown, L., Hu, Y., Yoshida, K., He, J., & Sun, T. (2019). Stable forearc stressed by a weak megathrust: Mechanical and geodynamic implications of stress changes caused by the $M = 9$ Tohoku-oki earthquake. *Journal of Geophysical Research: Solid Earth*, *124*(6), 6179–6194. https://doi.org/10.1029/2018JB017043

Wang, X., & Morgan, J. K. (2019). Controls on fore-arc deformation and stress switching after the Great 2011 Tohoku-oki earthquake from discrete numerical simulations. *Journal of Geophysical Research: Solid Earth*, *124*(8), 9265–9279. https://doi.org/10.1029/2019JB017420

Weng, H., & Ampuero, J.-P. (2019). The dynamics of elongated earthquake ruptures. *Journal of Geophysical Research: Solid Earth*, *124*(8), 8584–8610. https://doi.org/10.1029/2019JB017684

Wibberley, C. A., & Shimamoto, T. (2005). Earthquake slip weakening and asperities explained by thermal pressurization. *Nature*, *436*(7051), 689–692. https://doi.org/10.1038/nature03901

Wirp, S. A., Gabriel, A.-A., Madden, E. H., Schmeller, M., van Zelst, I., Krenz, L., et al. (2021). 3-D linked subduction, dynamic rupture, tsunami and inundation modeling: Dynamic effects of supershear and tsunami earthquakes, hypocenter location and shallow fault slip. *Frontiers in Earth Science*, *9*, 177. https://doi.org/10.3389/FEART.2021.626844

Wolf, S., Gabriel, A. A., & Bader, M. (2020). Optimization and local time stepping of an ADER-DG scheme for fully anisotropic wave propagation in complex geometries. In *Lecture Notes in Computer Science (Including Subseries Lecture Notes in Artificial Intelligence and Lecture Notes in Bioinformatics)* (LNCS, Vol. 12139, pp. 32–45). Springer. https://doi.org/10.1007/978-3-030-50420-5_3

Wollherr, S., Gabriel, A., & Mai, P. M. (2019). Landers 1992 "reloaded": Integrative dynamic earthquake rupture modeling. *Journal of Geophysical Research: Solid Earth*, *124*, 6666–6702. https://doi.org/10.1029/2018JB016355

Wollherr, S., Gabriel, A. A., & Uphoff, C. (2018). Off-fault plasticity in three-dimensional dynamic rupture simulations using a modal discontinuous Galerkin method on unstructured meshes: Implementation, verification, and application. *Geophysical Journal International*, *214*(3), 1556–1584. https://doi.org/10.1093/GJI/GGY213

Yao, S., & Yang, H. (2020). Rupture dynamics of the 2012 Nicoya M_w 7.6 earthquake: Evidence for low strength on the megathrust. *Geophysical Research Letters*, *47*(13). https://doi.org/10.1029/2020GL087508

Zhu, W., Allison, K. L., Dunham, E. M., & Yang, Y. (2020). Fault valving and pore pressure evolution in simulations of earthquake sequences and aseismic slip. *Nature Communications*, *11*(1), 1–11. https://doi.org/10.1038/s41467-020-18598-z